



UNIVERSITAT
POLITÈCNICA
DE VALÈNCIA

– **TELECOM** ESCUELA
TÉCNICA **VLC** SUPERIOR
DE INGENIERÍA DE
TELECOMUNICACIÓN

UNIVERSITAT POLITÈCNICA DE VALÈNCIA

School of Telecommunications Engineering

Photonic switches based on Sb₂Se₃/Si technology for
datacom applications

Master's Thesis

Master's Degree in Telecommunication Engineering

AUTHOR: Benacloche Llácer, Cristina

Tutor: Sanchis Kilders, Pablo

Experimental director: PARRA GOMEZ, JORGE

ACADEMIC YEAR: 2022/2023

Resumen

El objetivo de este trabajo fin de máster es el desarrollo de conmutadores electro-ópticos en tecnología Sb_2Se_3/Si . La implementación de materiales de cambio de fase (PCM) basados en calcogenuros puede realizar un cambio notable debido a que se tiene una respuesta de conmutación no volátil, la integración de este material de cambio de fase (Sb_2Se_3) en estructuras de silicio permite el desarrollo de dispositivos altamente compactos y con una funcionalidad de conmutación no-volátil. Esto es debido a que este material presenta un elevado cambio de índice de refracción que además no es volátil y con una absorción a frecuencias ópticas prácticamente despreciable. De esta forma, se pretende desarrollar una solución de conmutación electro-óptica innovadora y eficiente energéticamente que podría utilizarse en los centros de datos para tareas de procesamiento de información en el dominio óptico.

Resum

L'objectiu d'aquest treball fi de màster és el desenvolupament de conmutadors electro-òptics en tecnologia Sb_2Se_3/Si . La implementació de materials de canvi de fase (PCM) basats en calcogenurs pot fer un canvi notable pel fet que es té una resposta de commutació no volàtil, la integració d'aquest material de canvi de fase (Sb_2Se_3) en estructures de silici permet el desenvolupament de dispositius altament compactes i amb una funcionalitat de commutació no-volàtil. Això és pel fet que aquest material presenta un elevat canvi d'índex de refracció que a més no és volàtil i amb una absorció a freqüències òptiques pràcticament menyspreable. D'aquesta manera, es pretén desenvolupar una solució de commutació electro-òptica innovadora i eficient energèticament que podria utilitzar-se en els centres de dades per a tasques de processament d'informació en el domini òptic.

Abstract

The aim of this master's thesis is the development of electro-optical switches in Sb_2Se_3/Si technology. The implementation of chalcogenide-based phase change materials (PCM) can make a remarkable change due to their non-volatile switching response. The integration of this phase change material (Sb_2Se_3) in silicon structures allows the development of highly compact devices with non-volatile switching functionality. This is due to the fact that this material has a high refractive index change, is non-volatile, and has practically negligible absorption at optical frequencies. In this way, the aim is to develop an innovative and energy-efficient electro-optical switching solution that could be used in data centers for information processing tasks in the optical domain.

Contents

I Memory

1 Introduction	1
1.1 Motivation	1
1.2 Contribution to the SDGs	3
1.3 Objectives	4
1.3.1 Distribution of the document	4
1.4 Methodology	5
1.4.1 Project development	5
1.4.2 Gantt Chart	6
2 Design of the hybrid phase shifter	7
2.1 Description of hybrid waveguide and material properties	7
2.2 Design of hybrid waveguide: single mode condition for amorphous and crystalline states	8
2.2.1 Amorphous state	9
2.2.2 Crystalline state	12
2.3 Design of hybrid phase shifter and analysis of performance metrics	16
2.4 Comparison of methods for changing the material	21
2.5 Summary of final design	23
3 Design of the photonic switch device	24
3.1 Description of photonic switch device	24
3.1.1 Parameters of the switch to be analysed	24
3.1.1.1 Extinction ratio (ER)	24
3.1.1.2 Insertion losses (IL)	24
3.1.1.3 Crosstalk (CT)	25
3.1.2 Design of the photonic switch	25
3.1.2.1 Bar state	26
3.1.2.2 Cross state	26
3.2 Design of silicon bends and MMIs	28
3.2.1 Silicon bends	28
3.2.2 MMIs	30
3.3 Design of grating couplers for fiber coupling	35
3.4 Summary of final design	38
4 Fabrication and experimental results	39
4.1 Description of fabrication process	39

4.2	Mask design of testing devices	40
4.3	Selection of experimental set-up	42
4.4	Experimental results	42
5	Conclusions and future work	46
5.1	Conclusions	46
5.2	Future work	47
	References	49
II	Appendix	
A	Simulation with FemSIM	51
B	Simulations with FullWAVE	54
B.0.1	Spatial domain grid sizes	54
B.0.2	Time domain, time step and excitation	56

List of Figures

1.1	Data processing centers [2].	1
1.2	Advantages Sb_2Se_3 phase shifter [2].	2
1.3	Amorphous and crystalline states that can be achieved with the Sb_2Se_3 material [1].	3
1.4	Objective of the 2030 Agenda for Sustainable Development [7].	4
1.5	Gantt chart describing how the distribution of tasks has been carried out.	6
2.1	Sb_3Se_2 refractive indices for all wavelengths in both amorphous and crystalline states.	7
2.2	Hybrid waveguide dimensions.	9
2.3	Sweep varying the waveguide width from 200 nm to 600 nm state amorphous.	9
2.4	Simulation of the three modes of higher order for a waveguide width of 450 nm.	11
2.5	Hybrid waveguide structure without side guides.	11
2.6	TE ₀ and TM ₀ modes of the hybrid waveguide without the sides guides for a width of 450 nm.	11
2.7	Sweep varying the waveguide (without guide sides) width from 200 nm to 600 nm state amorphous.	12
2.8	Higher order modes of the hybrid waveguide without guide sides for a width of 450 nm for amorphous state.	12
2.9	Sweep varying the waveguide width from 200 nm to 600 nm state crystalline.	13
2.10	Simulation of the three modes of higher order for a waveguide width of 450 nm for crystalline state.	14
2.11	Sweep varying the waveguide (without guide sides) width from 200 nm to 600 nm state crystalline.	14
2.12	TE ₀ and TM ₀ modes of the hybrid waveguide without the sides guides for a width of 450 nm crystalline state.	15
2.13	Higher order modes of the hybrid waveguide without guide sides for a width of 450 nm for crystalline state.	15
2.14	Variation of refractive index with wavelength and values at 1310 nm.	16
2.15	Mode of the waveguide with a width of 450 nm at amorphous state.	16
2.16	Mode of the waveguide with a width of 450 nm at crystalline state.	16
2.17	Optical power loss in dB per unit length for crystalline state.	17
2.18	Phase shifter length to achieve a π phase shift as a function of the Si/Sb_2Se_3 waveguide width. Results are obtained considering a 40 nm thick Sb_2Se_3 layer and $\lambda = 1310$ nm.	18
2.19	Phase shifter length to achieve a π phase shift as a function of the Si/Sb_2Se_3 waveguide width.	18
2.20	Insertion losses associated with the 450 nm width of the wavelength.	19
2.21	View from above of the designed phase shifter.	20

2.22	E_x at state amorphous.	20
2.23	E_x at state crystalline.	20
2.24	Checking the π offset between the two states of the material.	21
2.25	Three-dimensional schematic of the proposed compact re-configurable silicon waveguide [10].	22
3.1	Design of the symmetric photonic switch to be made, consisting of two phase shifters designed in the previous chapter and two 2x2 splitter.	25
3.2	Description of how power is distributed through the switch in the bar state.	26
3.3	Description of how power is distributed through the switch in the cross state.	26
3.4	Estimation of the losses obtained in cross state.	27
3.5	Estimation of the losses obtained in bar state.	27
3.6	Structure of the bend.	28
3.7	Losses associated with different bending radius.	29
3.8	Real part of the effective index associated with different bending radius.	29
3.9	Simulation results for the radius values of 0.5, 2 and $5\mu m$	30
3.10	2x2 splitter to be analysed.	30
3.11	2x2 splitter to be analysed with the fixed dimensions.	31
3.12	2x2 splitter to be analysed with the fixed dimensions.	31
3.13	Final structure of the 2x2 splitter with taper.	32
3.14	2x2 splitter simulation result.	32
3.15	2x2 splitter insertion losses.	33
3.16	2x2 splitter excess losses.	34
3.17	2x2 splitter imbalance.	34
3.18	Schematic of the grating coupler.	35
3.19	Pitch of the grating coupler.	36
3.20	Fill factor of the grating coupler.	37
3.21	Overlap of the grating coupler.	37
4.1	Schematic of electro beam lithography process [11].	40
4.2	GDS structure of the sample to be tested.	41
4.3	Detailed view of copy no. 1 of the sample to be analysed.	41
4.4	Setup for characterisation of the sample (Schematic).	42
4.5	Inspection through the microscope of the TE test structure of copy 1.	43
4.6	Inspection through the microscope of the TE bend structure of copy 1.	43
4.7	Inspection through the microscope of the grating structure of copy 1.	43
4.8	GDS image for the straight TE polarisation structure.	44
4.9	Analysis of propagation losses as a function of waveguide length for the straight structure in TE polarisation.	44
4.10	Linear fit of propagation losses of waveguide length for the straight structure in TE polarisation.	45
A.1	Simulation area of the 2D structure simulated in FemSIM.	51
A.2	Required parameters to configure in FemSIM.	52
A.3	Mesh options parameters to configure in FemSIM.	52
A.4	Result of the mesh, after setting the necessary parameters.	53
B.1	Simulation area of the designed structure.	54

B.2	Configuration of spatial domain and grid size parameters.	55
B.3	A sample non-uniform of the waveguide. A fine grid size of 20 nm is used.	56
B.4	Parameters to be configured time domain, time step and excitation.	56
B.5	Index of the guide used as a launch in the simulation.	57
B.6	Distribution of the monitors used in the structure.	57

Index of tables

2.1	Refractive index of materials at $\lambda = 1310nm$	8
2.2	Calculation of the first two modes in the waveguide for a sweep from 200 nm to 500 nm for the amorphous state.	10
2.3	Calculation of the first two modes in the waveguide for a sweep from 200 nm to 500 nm for crystalline state.	13
3.1	Dimensions of the 2x2 splitter to be simulated.	33
4.1	Results of straight waveguide losses and grating couplers for TE polarisation.	45

Chapter 1

Introduction

1.1 Motivation

Nowadays, the relevance of communications in our lives, especially data communications, has increased exponentially. This has turned the matter of obtaining reliable data transmissions a top priority. Efficient data transmission and high speeds is a factor that is currently in great demand, especially at a wavelength of 1310 nm.

The motivation for conducting a study on photonics is that there have been recent advances in silicon photonic devices. These advancements have allowed devices to be ultra-compact, efficient, and with high bandwidth, as opposed to electronic devices, which are limited by bandwidth. Due to advances in photonic integrated circuits (PICs) based on phase change materials (PCMs), these devices have the potential to create near-future computing units and data storage, that will revolutionise the architecture of today's computers [1].

Another motivating aspect of this work is the increasing demand from companies involved in telecommunications, data centres, among others sectors for effective and secure data transmissions. To achieve this, a robust infrastructure is essential for this sectors. These improvements in infrastructure benefits not only the digital sectors but also other sectors such as health, finance, among many others.

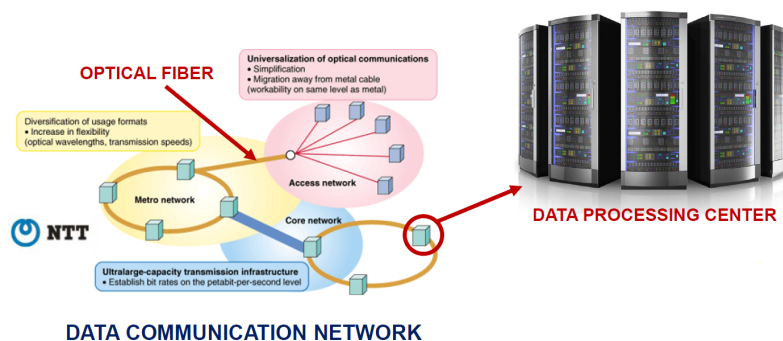


Figure 1.1: Data processing centers [2].

After explaining the different motivations, an explanation will be provided about what silicon integrated photonics consist of, the advantages of chalcogenides, and the material Sb_2Se_3 . First of all, silicon integrated devices allow the integration of several functionalities into a single device, thus becoming a point of great interest. This integration is achieved using the same mechanisms as the latest electronics. By introducing several functionalities into a single device, the price has reduce significantly. Silicon integrated photonic devices allow highly complex designs without significant costs increases, obtaining numerous benefits such as creating new opportunities that allow the transmission of data in a safe and efficient way through optical fibre.

On the other hand, integrated photonic systems have a wide variety of applications, apart from data communication, as explained above. Within these communications, we can find digital communications for several proposes [3]. However, data communication is not the only application of integrated photonics. There are currently a variety of new applications that are emerging, such as neuromorphic computing or biodetection [4] [5].

Integrated photonics is revolutionizing the field of optics, i.e. different integrated devices are being created from modulators, waveguides, detectors and more [3]. Among these devices, the Mach-Zehnder interferometer (MZIs) is commonly used due to achieve wide operating ranges. These devices take advantage of several effects, such as the thermo-optic effect, despite their considerable size, slower switching efficiency, and higher power consumption. Another effect used in these devices is the plasma dispersion effect, which slightly modifies the refractive index. In addition to, the electro-optical effect is employed, which has a faster speed but is less efficient in switching with the possibility of thermal drift problems.

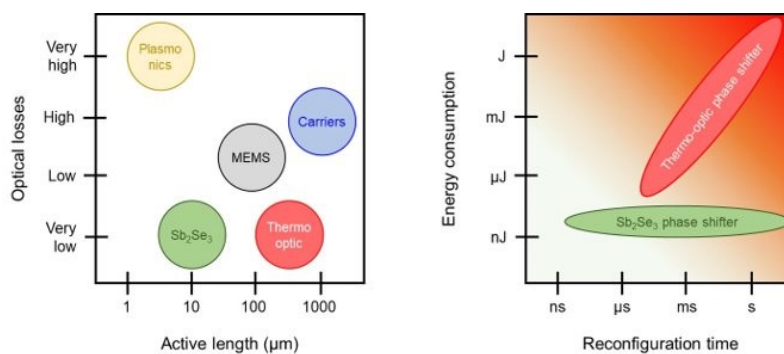


Figure 1.2: Advantages Sb_2Se_3 phase shifter [2].

Ideal integrated photonic devices should have a compact footprints, with the following characteristics. Firstly, a high switching speed. Secondly, a minimum consumption of both static and dynamic energy. With these ideal characteristics, the next step is to explain the devices based on phase change materials (PCM), which the characteristics of these devices make them ideal candidates to achieve good results.

PCM devices exhibits non-volatility, which allows the energy to hold the state to be approximately zero. There is high scalability, reaching nanometric dimensions, as well as, high refractive index contrast. Moreover, PCM devices demonstrate efficient switching, and a highly fast state change in units of nanoseconds. These materials are able to maintain stable states over a long period of time while enduring a large number of switching changes.

Overall, the most important characteristics of PCM, it can be concluded that they are the candidates

that get closely to the ideal characteristics of integrated photonic devices [1].

One of the characteristics explained above is the ability to switch the phase of the PCM material. This transition is achieved through different mechanisms. Firstly, the phase of the material can be accomplished using the thermal effect, which is carried out by external heaters using the Joule effect. On the other hand, the photothermal effect is used, which utilizes optical pulses. These mechanisms allows PCM have an impact on the switching performance of the devices. Therefore, it is crucial to choose the appropriate mechanism depending on the application [1].

The PCM chosen for this work is the antimony selenide (Sb_2Se_3). This material will be in an amorphous state and can be switched to a crystalline state by using heat. An overview of this transition to crystalline state is shown in figure 1.3. This heating process is a controlled transition of the material to the crystalline state [1].

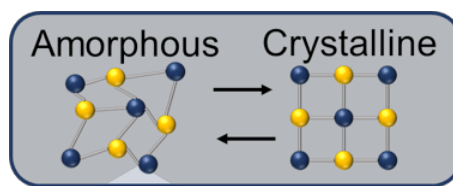


Figure 1.3: Amorphous and crystalline states that can be achieved with the Sb_2Se_3 material [1].

The other material used in this work is silicon (Si). This semiconductor material is highly used for the manufacturing of electronic devices due to its low cost and is easily available [6]. This material is transparent at optical frequencies, and for this reason it is normally used in the manufacture of waveguides and different optical devices.

Sb_2Se_3 has a high dielectric constant, which allows light to be confined in the waveguide. These properties make this material useful for the fabrication of waveguide layers in devices.

The use of the 1310 nm wavelength, it achieves scalable, robust, and efficient data transmissions, facilitating communication between devices, data centres and clients.

The use of the 1310 nm wavelength in the study of datacom provides different lines of research, requiring advances in signal processing, new modulation techniques, and thus to be able to make new advances in optical networks. This study can contribute to the development of new protocols and applications. Another reason for this design at 1310 nm is the ability to achieve negligible dispersion.

In conclusion, the main motivation of this work is to study these PCM, specially Sb_2Se_3 , and investigate their characteristics. The goal is to create devices with presents non-volatility, ultra-compact, high switching speed, low loss, and long-life stability. These devices aim to allow a significant reconfiguration of conventional static nanophotonic platforms.

1.2 Contribution to the SDGs

In the following section, we will discuss the potential contributions that the design and fabrication of the proposed device in this work could offer.

The Sustainable Development Goals (SDGs) are defined as actions to be taken to ending global poverty, protecting the planet, and improving human lives. World leaders have proposed a total of 17 goals [7], which can be summarised in the figure 1.4.



Figure 1.4: Objective of the 2030 Agenda for Sustainable Development [7].

Considering the SDGs, this work can be placed within the context of different objectives.

This work aligns with SDGs 7, *Ensure access to affordable, reliable, sustainable and modern energy*. The main advantage is the drastic reduction of energy consumption due to his ultra-compact size, in contrast to what happens with more conventional technologies. Additionally, this work contributes to SDG 9 and 12, called *Build resilient infrastructure, promote inclusive and sustainable industrialization and foster innovation* and *Ensure sustainable consumption and production patterns*.

In conclusion, this work involves several SDGs, making not only an innovative project but also could help to contribute to accomplishing the 2030 agenda.

1.3 Objectives

The aim of this Master's Thesis (TFM) is to develop photonic integrated switches based on Sb_2Se_3 technology. This TFM will focus on the design of each part of the photonic switch with special emphasis on the critical aspects of each component. It will also include an explanation of the design process and subsequent manufacture of the device. Finally, an analysis of the device will be presented.

1.3.1 Distribution of the document

This document will be organised in different chapters, which will be subdivided into several sections and subsections. The following section will provide a detail overview of how the document will be distributed.

- **Chapter 1: Introduction:** This chapter will explain the motivation for using the 1310 nm wavelength in data communication applications, as well as the layout of the document and

time distribution of the tasks carried out during the project.

- **Chapter 2: Design of hybrid phase shifter:** The most important characteristics of the material to be used, Sb_2Se_3 , will be explained, as well as the process used to design the hybrid phase shifter. This will be followed by the design of the phase shifter and an analysis of its optical response.
- **Chapter 3: Design of the photonic switch device:** This chapter explains the design of the different components that make up the switch and discusses all the design decisions taken to analyse the performance of the device.
- **Chapter 4: Fabrication and experimental results:** This chapter describes the manufacturing process used to validate the theoretical results compiled in previous chapters.
- **Chapter 5: Conclusions and future work:** This chapter will detail the conclusions drawn from the work and, at the same time, outline future lines of research.

1.4 Methodology

1.4.1 Project development

In this section, the methodology used throughout the stages will be explained. They can be divided into five stages. Firstly, a search and compilation of information was carried out, and at the same time, different bibliographic references were analysed. Then, we proceeded with the design of the phase shifter, whose design steps are explained in chapter two. In the third section, the design of the different components of the switch, such as the bend and multi mode interference coupler (MMI) is explained.

Then, in the fourth section, the experimental part of the project was carried out, for which the setup necessary to perform the experimental part and the necessary measurements to characterise the designed devices was assembled. Finally, this document was written, incorporating all the knowledge throughout the project.

- Task distribution:
 1. Review literature
 2. Design and simulations with RSoft simulator
 - (a) Analysis of Si/Sb_2Se_3 waveguide
 - i. Calculation of TE and TM modes
 - (b) Design of phase shifter
 - (c) Design of silicon bends and MMIs
 - (d) Design of grating couplers for fiber coupling
 3. Experimental characterisation of the device.
 4. Analysis and processing of the data obtained from both in the simulations and characterisation.
 5. Writing the report.

1.4.2 Gantt Chart

The following shows the timing of the tasks described above.

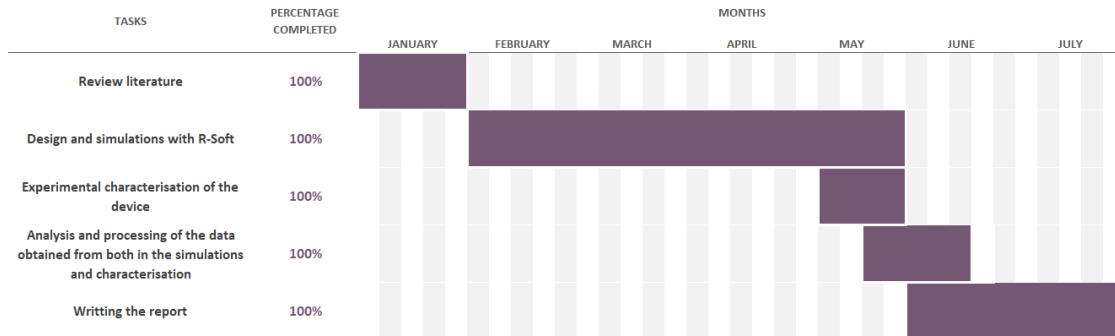


Figure 1.5: Gantt chart describing how the distribution of tasks has been carried out.

Chapter 2

Design of the hybrid phase shifter

2.1 Description of hybrid waveguide and material properties

In this section, we will explain how the waveguide was made and the most relevant characteristic properties of the phase change material to be used.

The first step to start the design is to know the refractive index of the material. In this case it was necessary to refer to the literature to obtain this information. Next, it will be present the graph extracted from [8], which allow us to determine the refractive index of Sb_2Se_3 .

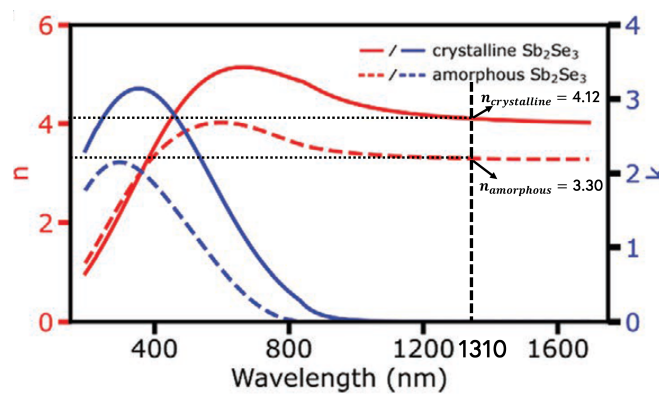


Figure 2.1: Sb_2Se_3 refractive indices for all wavelengths in both amorphous and crystalline states.

The refractive index of these materials is analysed below. As shown in the table 2.1, where the refractive index of the material are shown. In the case of Sb_2Se_3 , the refractive index varies depending on the state and the wavelength of light used.

On the other hand, the amorphous state has a refractive index of about 3.305 at 1310 nm, while the refractive index of crystalline state at this wavelength is about $4.121+0.001j$.

At a wavelength of 1310 nm, which is in the near-infrared region, the refractive index of silicon is 3.444.

Wavelength	Air	SiO_2	Si	Sb_2Se_3 (Amorphous)	Sb_2Se_3 (Crystalline)
1310 nm	1	1.444	3.5	3.305	4.121+0.001j

Table 2.1: Refractive index of materials at $\lambda = 1310nm$

Silicon oxide (SiO_2) is a dielectric material widely used in the fabrication of optical devices, including optical waveguides. At a wavelength of 1310 nm, which is in the near-infrared region, the refractive index of SiO_2 is approximately 1.45.

In the Si/Sb_2Se_3 waveguide, the Sb_2Se_3 layer is deposited on top of the silicon layer. The top layer that has been deposited is antimony selenide. This phase change material is an active material, so it has been placed right on top of the waveguide, the result is a strong interaction between the optical mode and the phase change material Sb_2Se_3 .

The Si/Sb_2Se_3 waveguide is used in applications where a high degree of control over the propagation of light in a small structure is required. SiO_2 is an optical wavelength transparent material and has high thermal and chemical resistance, making it ideal for use in optical waveguides and other optical devices.

2.2 Design of hybrid waveguide: single mode condition for amorphous and crystalline states

In the following, we will explain the process followed in the design of the hybrid waveguide, as well as determining the single mode condition of the amorphous and crystalline states.

Firstly, in the design of hybrid waveguides, it is important to consider the single mode conditions for the amorphous and crystalline states of the materials being used. The single mode condition ensures that only a single optical signal propagates in the waveguide, which improves the transmission quality.

To achieve the single mode condition, the difference in refractive indices between the top layer and the substrate must be large enough to ensure single mode propagation. Additionally, the ratio between the thickness of the top layer and the wavelength of the optical signal must also be considered to ensure single-mode propagation.

In the case of a hybrid waveguide consisting of an amorphous antimony selenide top layer on a silicon waveguide, the single-mode condition for the propagation of optical signals in both amorphous and crystalline states can be obtained by carefully tuning of the design parameters. For this reason, the initial dimensions of the waveguide must be determined, and a picture of the hybrid waveguide dimensions is shown below.

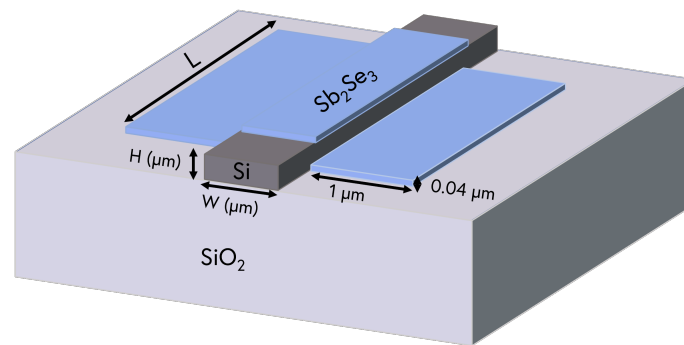


Figure 2.2: Hybrid waveguide dimensions.

As can be seen in the picture there is a SiO_2 layer on top of this layer. There is a hybrid waveguide which can be decomposed depending on the waveguide material.

- Si : The dimensions correspond to the standard value used in a commercial silicon on insulator wafer.
- Sb_2Se_3 : This material shall be placed on the two sides of the waveguide with a width of 1000 nm and a height of 40 nm, then a layer of Sb_2Se_3 shall be placed on top of the silicon layer with the same height of 40 nm.

Once the waveguide dimensions have been determined, the single-mode condition will be analysed using the refractive indices.

2.2.1 Amorphous state

A sweep is performed using the RSoft tool called MOST, varying the waveguide width from 200 nm to 600 nm, for the two states of antimony selenide (amorphous and crystalline).

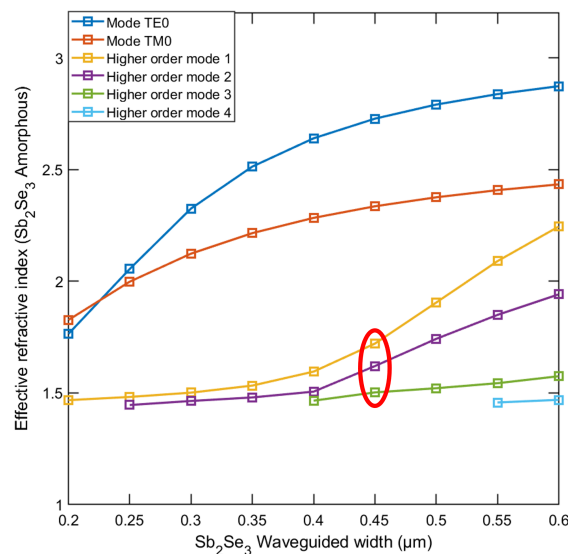


Figure 2.3: Sweep varying the waveguide width from 200 nm to 600 nm state amorphous.

The following table shows the first two modes obtained at different widths, starting with the amorphous state.

The configuration of the following simulations, with all the parameters to be set in RSoft, can be found in Appendix A.

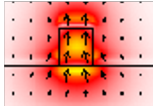
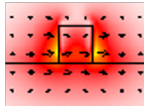
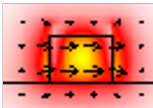
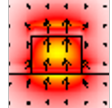
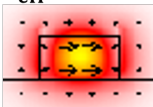
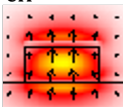
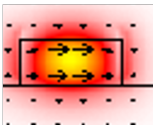
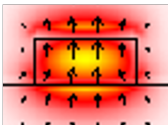
Width	Mode 1	Mode 2
200 nm	<p>Mode TM0 $n_{\text{eff}} = 1.826$</p> 	<p>Mode TE0 $n_{\text{eff}} = 1.764$</p> 
300 nm	<p>Mode TE0 $n_{\text{eff}} = 2.325$</p> 	<p>Mode TM0 $n_{\text{eff}} = 2.123$</p> 
400 nm	<p>Mode TE0 $n_{\text{eff}} = 2.639$</p> 	<p>Mode TM0 $n_{\text{eff}} = 2.283$</p> 
500 nm	<p>Mode TE0 $n_{\text{eff}} = 2.79$</p> 	<p>Mode TM0 $n_{\text{eff}} = 2.375$</p> 

Table 2.2: Calculation of the first two modes in the waveguide for a sweep from 200 nm to 500 nm for the amorphous state.

As will be explained in detail in the next section, the waveguide width has been defined as 450 nm. One of the reasons for choosing this waveguide width is to ensure a single-mode waveguide. However, it can be seen in figure 2.3 that the waveguide width is 450 nm. The waveguide is perceived to be non-single mode because there are three higher order modes. Nevertheless, as shown below, two of the modes don't have the light confined in the waveguide, while the third one doesn't have a linear polarization.

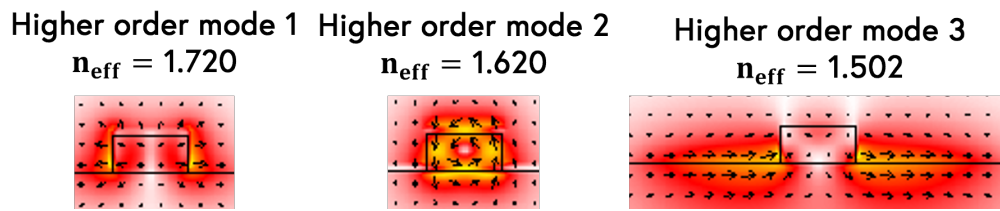


Figure 2.4: Simulation of the three modes of higher order for a waveguide width of 450 nm.

Next, the same hybrid waveguide shown in figure 2.2 will be simulated, with the difference that the side waveguides of the material will not be inserted Sb_2Se_3 . The schematic used will be shown below.

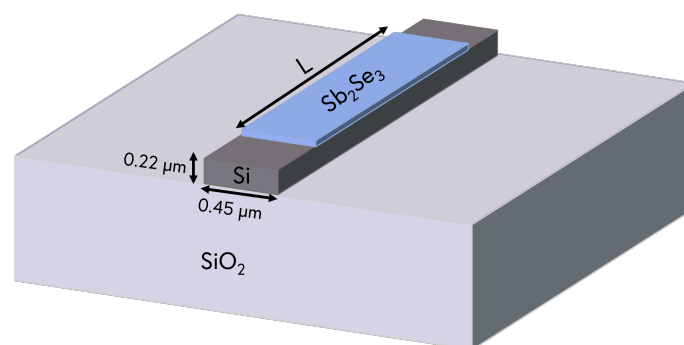


Figure 2.5: Hybrid waveguide structure without side guides.

There will be an analysis of what the modes should be for the waveguide width that has been set, 450 nm.

Firstly, the following figure shows the first two modes that appear: TE0 and TM0 modes. Their effective index are as follows:

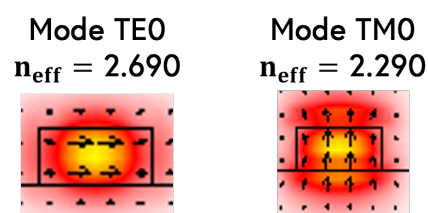


Figure 2.6: TE0 and TM0 modes of the hybrid waveguide without the sides guides for a width of 450 nm.

Next, the appearance of the higher order modes are shown, for which a sweep has been made from 0.2 to 0.6 to examine the behaviour of these higher order modes.

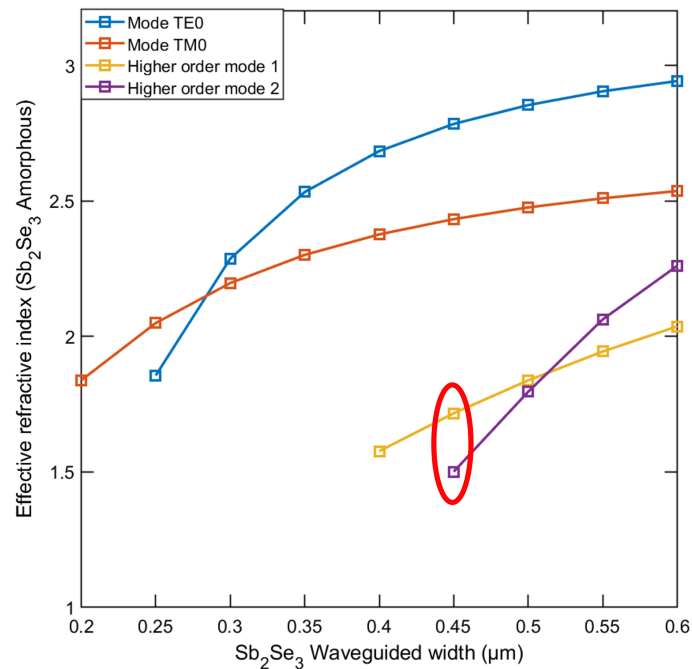


Figure 2.7: Sweep varying the waveguide (without guide sides) width from 200 nm to 600 nm state amorphous.

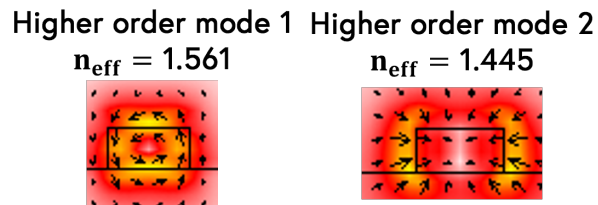


Figure 2.8: Higher order modes of the hybrid waveguide without guide sides for a width of 450 nm for amorphous state.

After analysing the hybrid waveguide with Sb_2Se_3 material guides on the side and without them, it can be concluded that in both cases, for a waveguide width of 450 nm, a single-mode waveguide is obtained. However, in this case, it will be used with side waveguides to make sure that there are no possible dispersion during the manufacturing process.

2.2.2 Crystalline state

In the following, the same waveguide design will be analysed but now for the crystalline state. Starting with the waveguide with side guides, followed by the analysis of the waveguide without side guides.

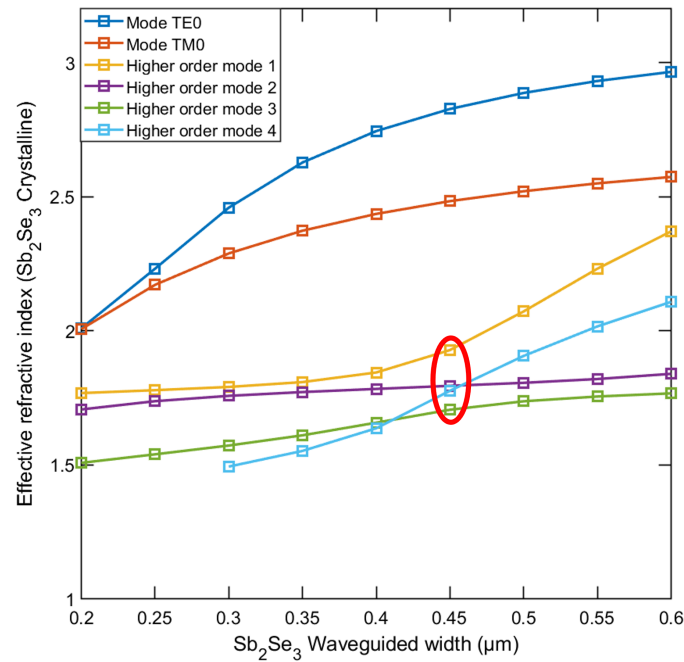


Figure 2.9: Sweep varying the waveguide width from 200 nm to 600 nm state crystalline.

The following table shows the first two modes obtained at different widths in the crystalline state.

Width	Mode 1	Mode 2
200 nm	$n_{\text{eff}} = 2.009$ 	$n_{\text{eff}} = 2.006$
300 nm	Mode TE0 $n_{\text{eff}} = 2.459$ 	Mode TM0 $n_{\text{eff}} = 2.288$
400 nm	Mode TE0 $n_{\text{eff}} = 2.744$ 	Mode TM0 $n_{\text{eff}} = 2.439$
500 nm	Mode TE0 $n_{\text{eff}} = 2.886$ 	Mode TM0 $n_{\text{eff}} = 2.520$

Table 2.3: Calculation of the first two modes in the waveguide for a sweep from 200 nm to 500 nm for crystalline state.

As mentioned above, the following chapter will explain why the width of the waveguide has been

chosen to be 450 nm. This width ensures a single-mode waveguide. However, it can be observed that in figure 2.9. For a width of 450 nm, initially might appear that this width provides multi-mode waveguide. However, as demonstrated below, there are three higher order modes, but these modes are dispersive.

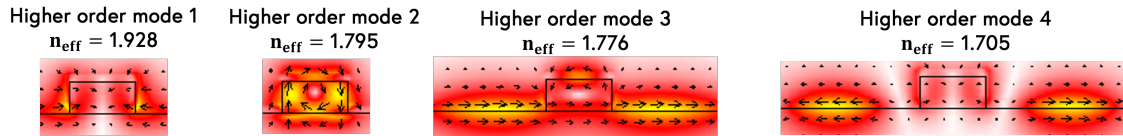


Figure 2.10: Simulation of the three modes of higher order for a waveguide width of 450 nm for crystalline state.

The same structure design without sides guides, as shown in the figure 2.5, will now be used to study the modes for a width of 450 nm.

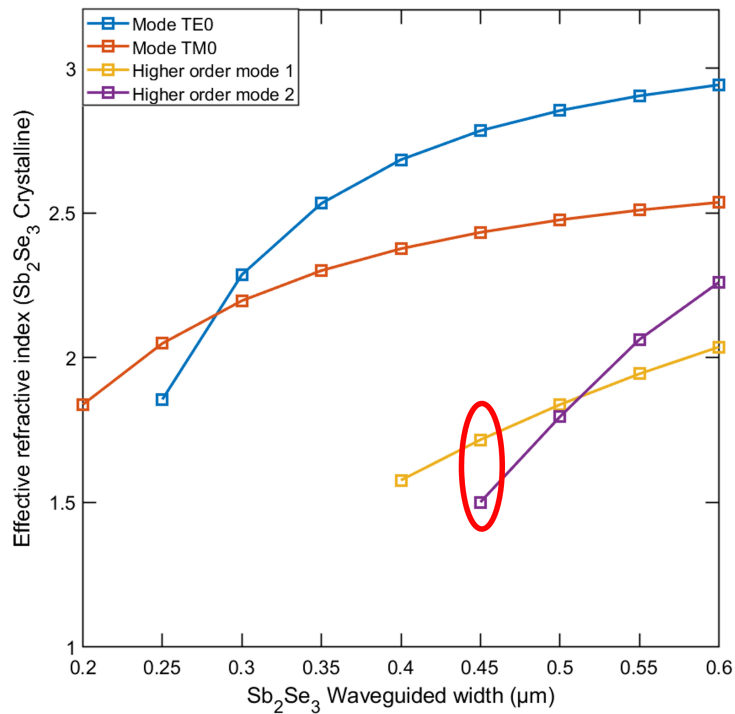


Figure 2.11: Sweep varying the waveguide (without guide sides) width from 200 nm to 600 nm state crystalline.

First of all, the first two modes that appear will be shown, which in this case are TE0 mode and TM0 mode, with their respective effective indices as shown below.

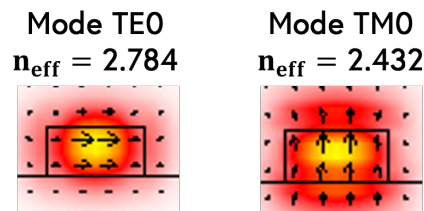


Figure 2.12: TE0 and TM0 modes of the hybrid waveguide without the sides guides for a width of 450 nm crystalline state.

The next step is to analyse the higher-order modes for the waveguide without side guides. The following modes are obtained.

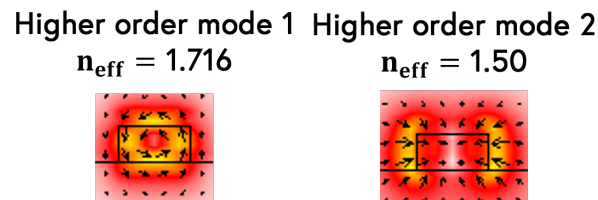


Figure 2.13: Higher order modes of the hybrid waveguide without guide sides for a width of 450 nm for crystalline state.

As can be seen in both the amorphous and crystalline state, using a 450 nm waveguide provides a single-mode waveguide condition. Therefore, this width will be used for the design of the phase shifter, which will be explained in the following chapter. In addition, a waveguide with sides guides of Sb_2Se_3 material shall be used to avoid possible dispersion.

As mentioned previously, the waveguide width will be 450 nm. After that, a wavelength-dependent sweep of the effective index will be performed in order to determine the effective index at 1310 nm for the different states.

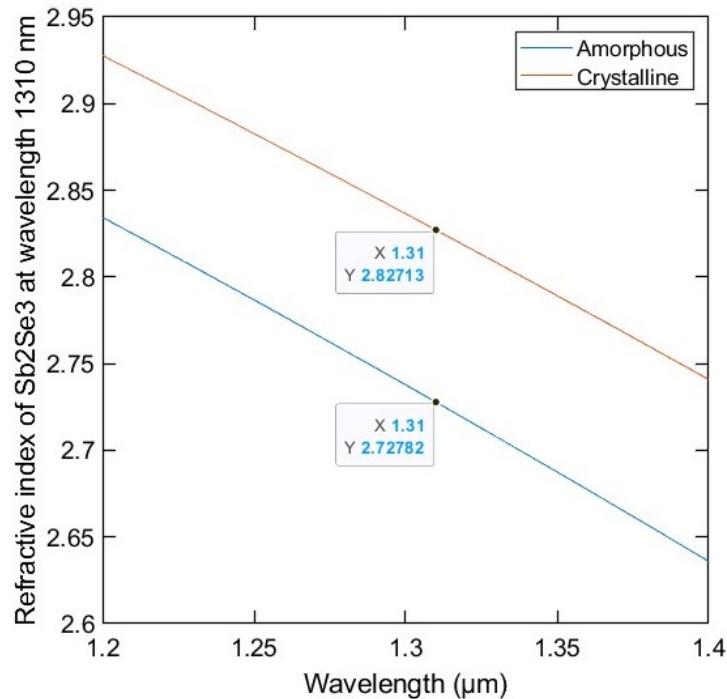


Figure 2.14: Variation of refractive index with wavelength and values at 1310 nm.



Figure 2.15: Mode of the waveguide with a width of 450 nm at amorphous state.

Figure 2.16: Mode of the waveguide with a width of 450 nm at crystalline state.

From the above figures, the effective index are determined 2.73 and 2.83 for the amorphous and crystalline state respectively.

2.3 Design of hybrid phase shifter and analysis of performance metrics

In this section, we will go ahead to design the hybrid phase shifter. As observed in the previous section, the crystalline state presents the most significant limitations. To determine the optimal mode for the phase shifter, as well as the associated optical losses, it is necessary to determine the exact length for a phase shift of π . Additionally, the insertion losses associated with the mode and the length of the waveguide chosen in this same section will be analysed. Once all these parameters are determined, the corresponding simulation will be conducted to confirm the designed values.

Firstly, the most suitable mode should be chosen by calculating the optical power loss in dB per

unit length using the following expression.

$$\alpha\left(\frac{dB}{\mu m}\right) = 20 \log_{10}(e) * 2\pi * \frac{\kappa_{eff}}{\lambda} \quad (2.1)$$

The following graph is presented below:

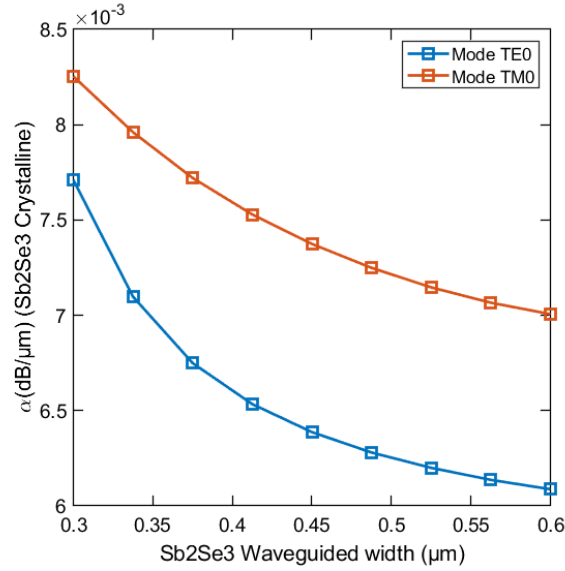


Figure 2.17: Optical power loss in dB per unit length for crystalline state.

As can be seen in the following graph, the TE0 mode presents the lowest optical losses. The next step is to select the appropriate waveguide length to achieve an offset of π .

To calculate the length of the phase shifter, the following expressions will be used for both TE0 and TM0 modes.

$$L_{\pi TE0} = \frac{\lambda}{2 * (n_{TE0_{crystalline}} - n_{TE0_{amorphous}})} \quad (2.2)$$

$$L_{\pi TM0} = \frac{\lambda}{2 * (n_{TM0_{crystalline}} - n_{TM0_{amorphous}})} \quad (2.3)$$

The graph below is obtained.

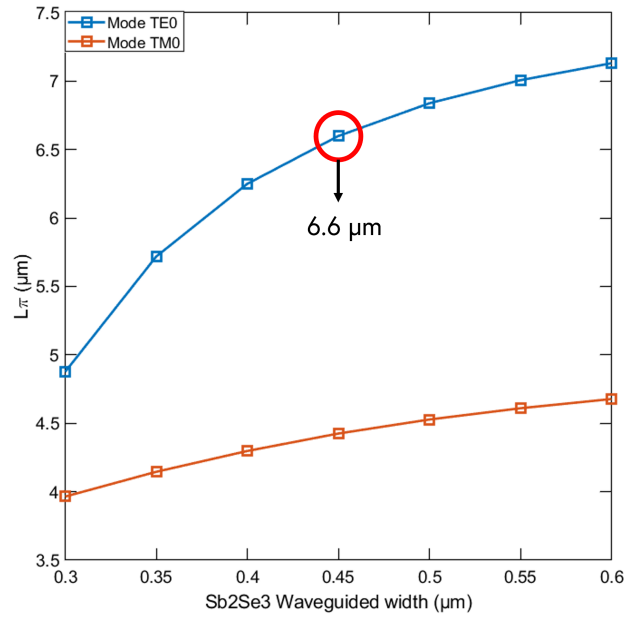


Figure 2.18: Phase shifter length to achieve a π phase shift as a function of the Si/Sb_2Se_3 waveguide width. Results are obtained considering a 40 nm thick Sb_2Se_3 layer and $\lambda = 1310$ nm.

As observed in the figure above and according to the data collected from the simulations, it can be determined that for a width of 450 nm, the length of the hybrid waveguide required for a phase shift of π must be $6.6 \mu m$.

Next, to confirm that the distance obtained in the previous graph is correct, an analysis is performed to obtain a different phase shift value depending on the length of the hybrid waveguide.

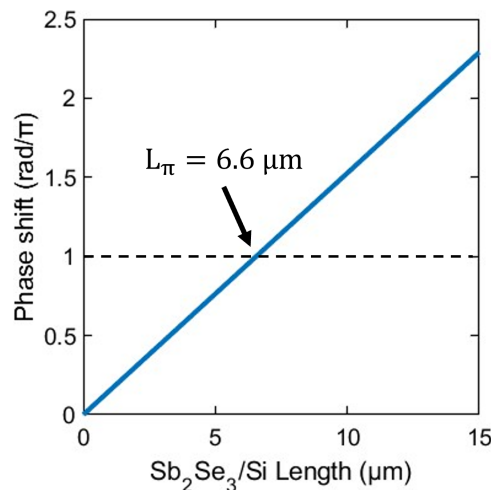


Figure 2.19: Phase shifter length to achieve a π phase shift as a function of the Si/Sb_2Se_3 waveguide width.

As can be seen in both figures 2.18 and 2.19, both confirm that for a length of $6.6 \mu\text{m}$, a phase shift of π is obtained. Subsequently, we will validate this desired phase shift through simulation.

Finally, the insertion loss (IL) associated with the 450 nm waveguide width will be analysed, and the following mathematical expression will be used to calculate this insertion loss.

$$IL(\text{dB}) = L_{\pi}(\mu\text{m}) * \alpha_{\text{crystalline}}\left(\frac{\text{dB}}{\mu\text{m}}\right) \quad (2.4)$$

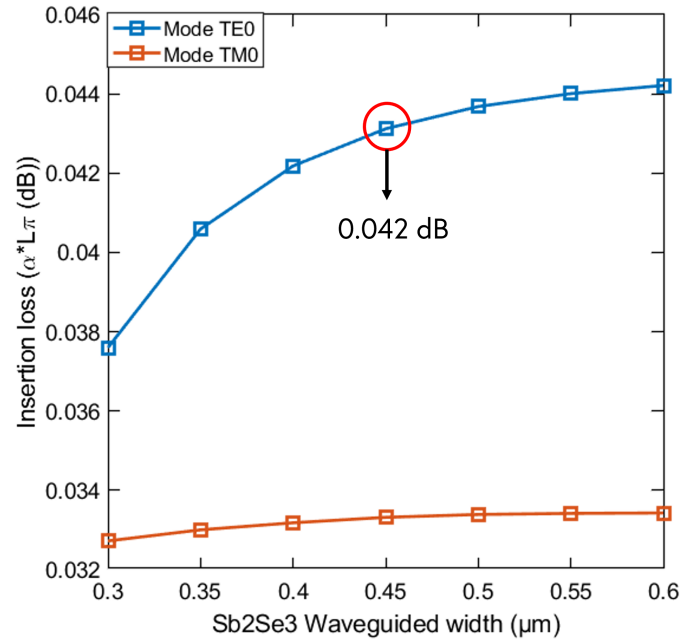


Figure 2.20: Insertion losses associated with the 450 nm width of the wavelength.

After determining the length of the waveguide that provides us acceptable losses for our design, we will verify if this length provides us an offset of π . This verification will be performed using the finite difference time domain (FDTD) method. The design to be simulated and its dimensions can be seen in the image shown below.

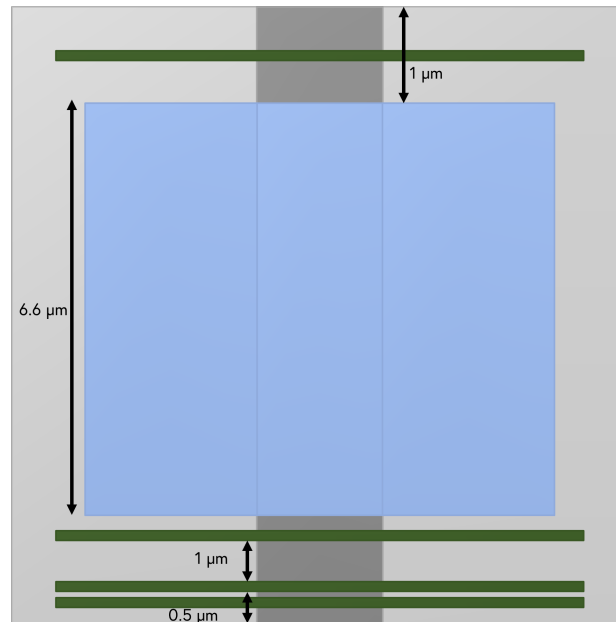


Figure 2.21: View from above of the designed phase shifter.

This waveguide has been simulated under the following simulation conditions: 10-point division in the X, Y and Z axes, and a grid size of 20 nm in the X and Y components. Please refer to Appendix 2 for an explanation of the FullWAVE simulations.

Once the simulation is finished, the following results are obtained:

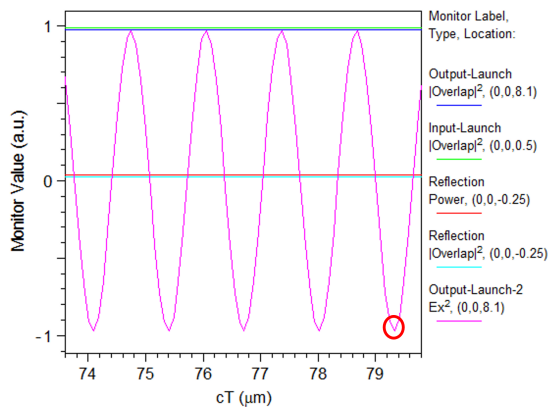


Figure 2.22: E_x at state amorphous.

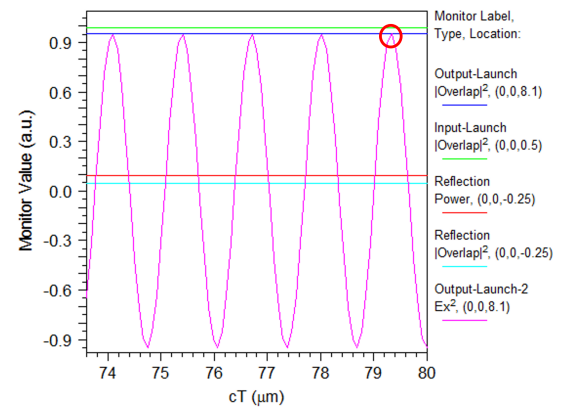


Figure 2.23: E_x at state crystalline.

A cross-section of the waveguide is shown below, where it can be seen the π phase shift between the two states of the material.

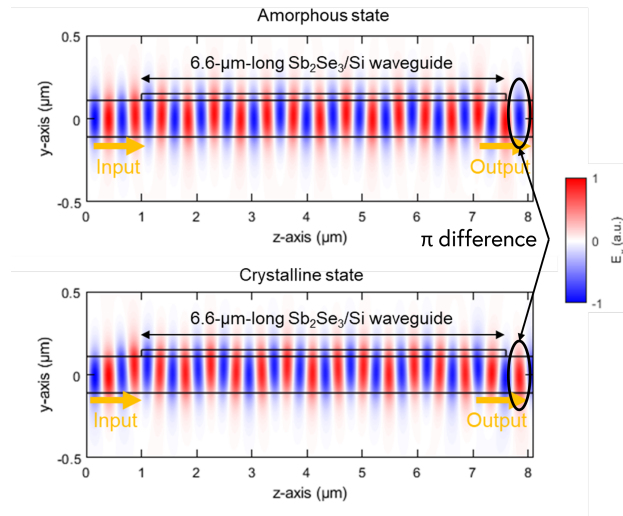


Figure 2.24: Checking the π offset between the two states of the material.

2.4 Comparison of methods for changing the material

The phase change material Sb_2Se_3 is a highly fascinating material for optoelectronic devices due to its ability to switch reversibly between two solid states: amorphous and crystalline. Extensive research in phase change materials focuses on their ability to transition between the amorphous to crystalline solid state, which can be achieved by applying several stimulate, such as electrical, thermal, or optical pulses.

The material Sb_2Se_3 has been extensively investigated due to its intrinsic properties, such as its high switching capacity, low absorption coefficient and high thermal stability. Typically, the material is deposited on a silicon layer and covered with a SiO_2 capping layer to protect it and improve its thermal stability.

The amorphous state is characterised by a disordered structure, while the crystalline state is characterised by an ordered structure. These two states exhibit distinct optical and electrical properties, making them suitable for use in different applications.

To induce the state change of the Sb_2Se_3 material, electrical pulses of different lengths and powers were employed. The rate of state change was characterised using optical spectroscopy and electron microscopy techniques. In addition, a laser with a wavelength of 488 nm was used to study the behaviour of the Sb_2Se_3 material under the influence of an optical pulse.

To transition the material from amorphous to crystalline state, an electric pulse of 12 mW was applied for a duration of one second. During this time, the temperature of the material increases, which induces the transition from the amorphous to the crystalline state. The transition can be monitored by measuring the optical transmission of the material.

To transition the material from crystalline to the amorphous state, a pulse with a variable pulse length of 60 mW was used [9]. The high intensity pulse leads to a rapid temperature increase in the material, which induces the transition from the crystalline to the amorphous state. The pulse length was adjusted to determine the time required for the transition.

It is important to note that the transition between amorphous to crystalline is reversible and can be repeated numerous times. The state change temperature of the material is 170°C , which means that the transition from amorphous to crystalline can be induced at this temperature. The material has a melting point of 610°C .

Reported results indicate that the material Sb_2Se_3 exhibits the ability to change from amorphous to crystalline and vice versa in a repetitive manner. In addition, it has observed that the wavelength of the laser light used to measure the state change of the material can influence the rate of state change. Moreover, the application of a SiO_2 coating on the Sb_2Se_3 material has been found to enhance its stability and durability compared to the Sb_2Se_3 material.

Furthermore, the literature indicates that there an alternative method to achieve the state change [10]. The reported work focuses on a new design of reconfigurable and ultra-compact silicon waveguide mode converters based on non-volatile optical phase change materials. It describes a new approach for mode conversion in silicon waveguides using non-volatile optical phase change materials. The aim of this approach is to increase the efficiency and reduce the size of the mode converter. Optical phase-shift materials have the ability to modify the optical properties of a material in response to an external stimulate, in this case, an electrical pulse [10].

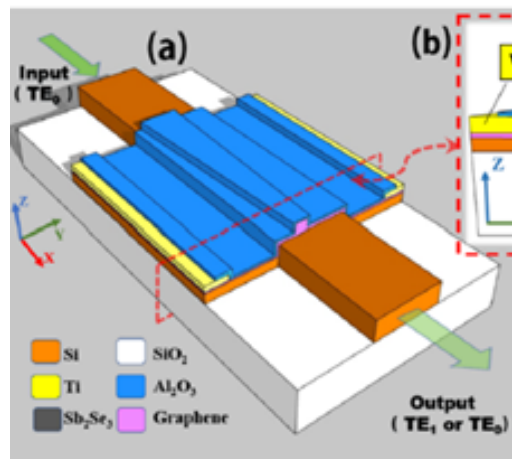


Figure 2.25: Three-dimensional schematic of the proposed compact re-configurable silicon waveguide [10].

In addition, the researchers used graphene as the microheater in the device. Graphene is a material with high thermal conductivity and low heat capacity, which makes it an excellent micro-heater. It was employed to heat the Sb_2Se_3 thin film, facilitating the transition between amorphous and crystalline. The pulse width required for the transition from amorphous to crystalline state was found to be $100 \mu\text{s}$, while the transition from crystalline to amorphous state required a pulse width of 400 ns .

In terms of geometry, the design uses a 20 nm thickness of aluminium oxide (Al_2O_3) layer, a 0.35 nm thickness of graphene layer (which acts as an efficient micro-heater due to its high thermal conductivity and low heat capacity), a metal electrode layer with a thickness of 100 nm , and a silicon plate layer with a thickness of 50 nm to facilitate rapid heat dissipation when the Sb_2Se_3 layer changes from amorphous to crystalline state. The silicon waveguide has a width of $1.1 \mu\text{m}$ and a thickness of 220 nm .



In terms of power consumption, a pulse width of $100 \mu s$ is required to transition from amorphous to crystalline state, while a pulse width of $400 ns$ is required to transition from crystalline to amorphous state. A switching cycle from one state to another of $250 \mu s$. The micro-heater employed for this purpose is graphene, and the state change occurs at a temperature of $200^\circ C$, while the melting temperature is $619^\circ C$ [10].

The use of graphene as a micro-heater offers an efficient way to change the state of the optical phase-change material. The resulting device is compact and efficient in terms of power consumption and switching speed.

2.5 Summary of final design

This section will explain the final conclusions of the design. The design of a hybrid phase shifter at $1310 nm$ has been successfully accomplished. After determining the desired the state of Sb_2Se_3 to be used, the relevant parameters were calculated. Obtaining the following results, we obtained optical power losses around $0.0064 dB/\mu m$ for the TE0 mode. Subsequently, the required length for achieving a phase shift of π was calculated, obtaining that the length for the waveguide width that has been established is $6.6 \mu m$. With the length was established, the insertion losses were calculated and found be $0.043 dB$. Finally, it was verified that there was a phase shift of π for the length established.

Chapter 3

Design of the photonic switch device

This chapter details the design process of the photonic switch device, covering important parameters and component design, including bends, MMIs, and grating couplers.

3.1 Description of photonic switch device

This section focuses on the design of the photonic switch. A non-volatile 2x2 Mach-Zehnder interferometer (MZI) switch based on the previous phase shifter is proposed. The phase shifters are placed on both arms of the MZI, the amount of optical power of each output can be controlled by configuring the state of the phase shifters.

The most important parameters for switch design are explained below.

3.1.1 Parameters of the switch to be analysed

3.1.1.1 Extinction ratio (ER)

The extinction ratio (ER) is expressed as follows:

$$ER = \frac{P_1}{P_2} \quad (3.1)$$

This value is typically expressed in dB or linear units. The extinction ratio indicates the relationships between the output power when the switch is 'on' and the output power when the switch is off. As the higher ER value indicates a better performance.

$$ER(dB) = 10 \log_{10} \left(\frac{P_{max}}{P_{min}} \right) \quad (3.2)$$

3.1.1.2 Insertion losses (IL)

Another important parameter is the insertion loss (IL), which refers when the switch is in the 'on' state.

Another approach to explain how insertion loss are defined is the sum of several losses, including coupling losses, propagation losses and absorption losses. The expression defining this parameter is as follows.

$$IL(dB) = -10\log_{10}\left(\frac{P_{out}}{P_{in}}\right) \quad (3.3)$$

Where P_{out} is the output power and P_{in} is the input power.

3.1.1.3 Crosstalk (CT)

Finally, another important parameter is the crosstalk, CT. It is essential to discuss crosstalk CT considering the switch's specifications, as it describes any undesired effect that occurs when a signal transmitted over a single circuit or channel of a transmission system interferes an undesirable effect in a different circuit or channel. Crosstalk is often caused by unintentional coupling from one circuit, section of a circuit, or channel to another.

According to the definition, this is the ratio of power at a specific output.

$$CT(dB) = 10\log_{10}\left(\frac{P_{output_n}}{P_{in}}\right) \quad (3.4)$$

3.1.2 Design of the photonic switch

Having explained the different parameters to be considered account when designing this device, we will now show a figure showing how the design to be carried out is laid out.

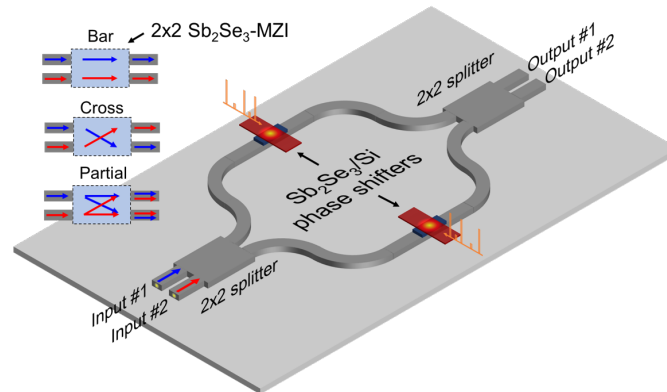


Figure 3.1: Design of the symmetric photonic switch to be made, consisting of two phase shifters designed in the previous chapter and two 2x2 splitter.

As can be seen in the figure 3.1 this 2x2 MZI is composed of two-phase shifters described in the previous chapter, as well as two 2x2 splitter at the beginning and end of the device. This component will be described in the next section.

In figure 3.1 the different configurations that the photonic switch can have are shown, denominated bar and cross state. Subsequently, an explanation of these two configurations will be provided.

3.1.2.1 Bar state

This means that the switch is in the bar state, when the light enters port 1 and exits port 1, as illustrated in the following figure.

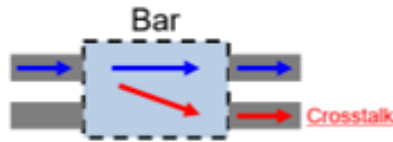


Figure 3.2: Description of how power is distributed through the switch in the bar state.

In the bar state, all the power entering port 1 is directed to output port 1, while there may be minimal coupling losses observed at output port 2.

3.1.2.2 Cross state

This means that the switch is in the cross state, where the light enters port 1 and exits port 2, as shown in the following figure.

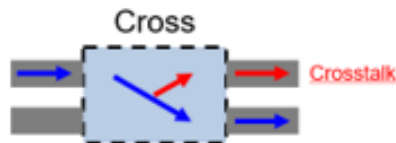


Figure 3.3: Description of how power is distributed through the switch in the cross state.

In the cross state, all the power entering port 1 is directed to output port 2, while there may be minimal coupling losses observed at port 1.

The losses obtained in each of the states have been estimated below.

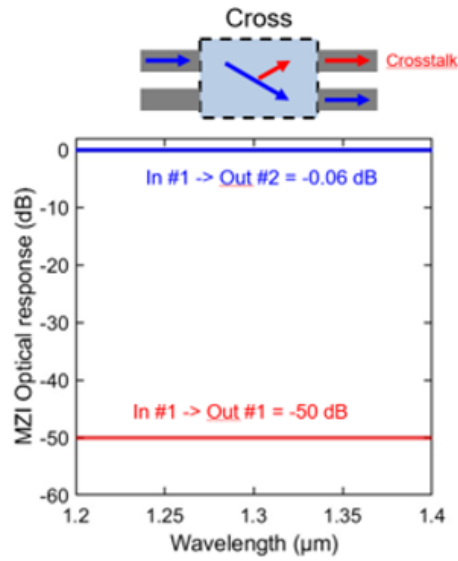


Figure 3.4: Estimation of the losses obtained in cross state.

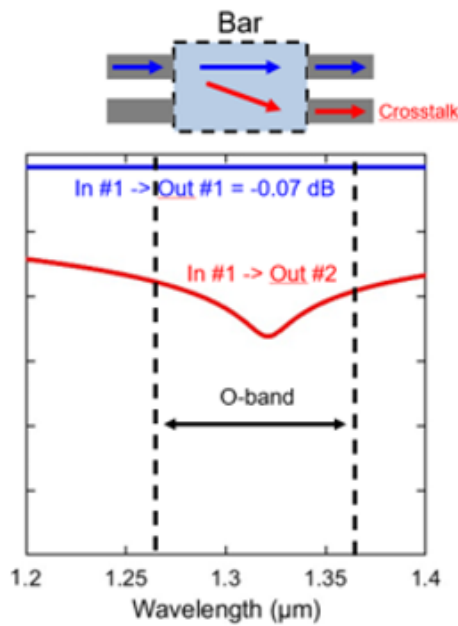


Figure 3.5: Estimation of the losses obtained in bar state.

As can be seen in figures 3.4 3.5, in the bar state, the losses obtained by output port 1 are approximately -0.07 dB, while in the cross state, these losses are approximately -0.06 dB. In both cases, the losses from the other output port tend to be infinite.

3.2 Design of silicon bends and MMIs

In this section we will explain the design of the different elements that comprise the switch shown above. Firstly, we will discuss the radius of the bend chosen, followed by an analysis of the MMI used.

3.2.1 Silicon bends

As can be seen in figure 3.1 it is composed of several bends. In this section, we will explain which radius has been chosen, taking into account the data obtained from the simulations.

The simulated structure is shown below:

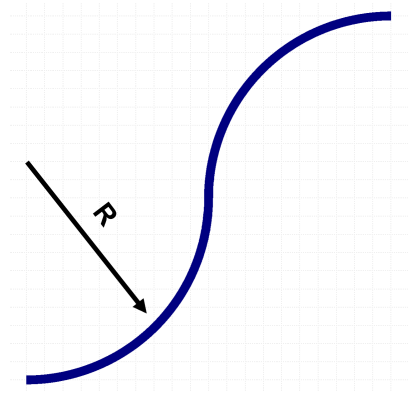


Figure 3.6: Structure of the bend.

In this section, the design process that was followed to design the bend to be used in the structure will be explained.

First, a sweep will be carried out for a range of different radius values. Particularly for the following interval $[0.5-10] \mu\text{m}$, a graph will be obtained from this sweep. An optical mode is obtained, which will show the losses for different radius. To calculate the total losses along the entire curve, the expression will be following:

$$Total Losses(dB) = \frac{\pi}{2} * R(\mu\text{m}) * \alpha\left(\frac{dB}{\mu\text{m}}\right) \quad (3.5)$$

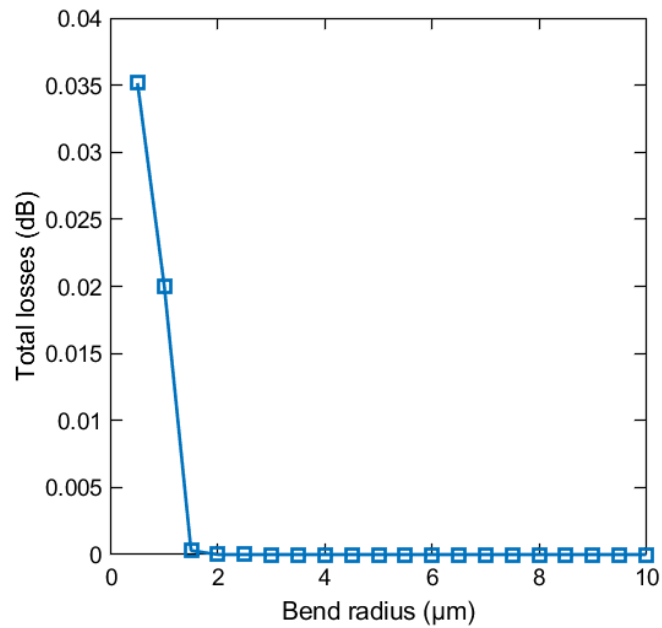


Figure 3.7: Losses associated with different bending radius.

Figure 3.7 illustrate that for a radius of $2 \mu\text{m}$, the obtained losses are negligible. On the other hand, the results demonstrate that the effective index remains the same as in a straight waveguide for values above $5 \mu\text{m}$. However, differences in the effective index value between the straight waveguide and the curve can potentially result in mode decoupling losses.

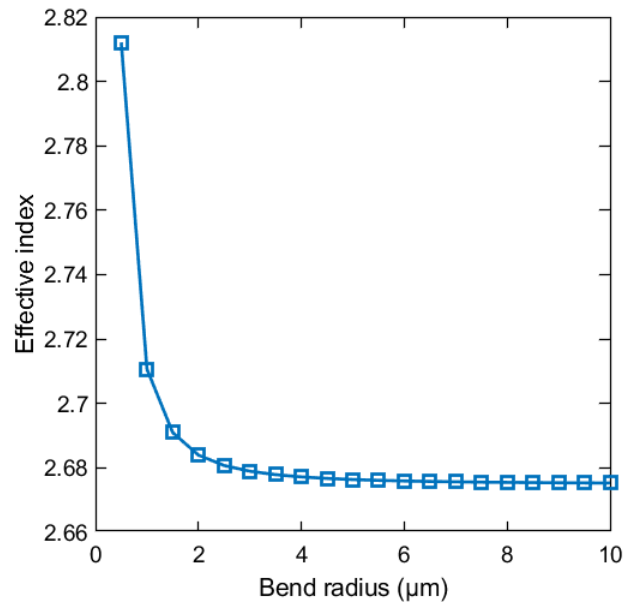


Figure 3.8: Real part of the effective index associated with different bending radius.

A simulation was performed using RSoft for three different radius values: 0.5, 2 and 5 μm . The results obtained for each of these radius values are presented below.

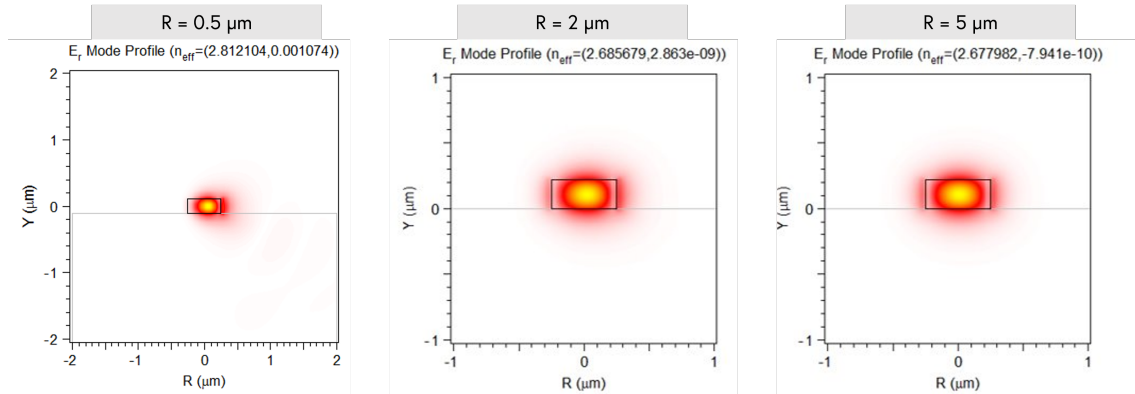


Figure 3.9: Simulation results for the radius values of 0.5, 2 and 5 μm .

As shown in Figure 3.7, 3.8 and 3.9, the effective index simulation remains nearly the same from a radius of 5 μm . Therefore, it has been determined that a radius of 5 μm is chosen for the design of the bend.

3.2.2 MMIs

This section will explain the design process for the 2x2 MMI. First, we will present a figure illustrating the structure of this element.

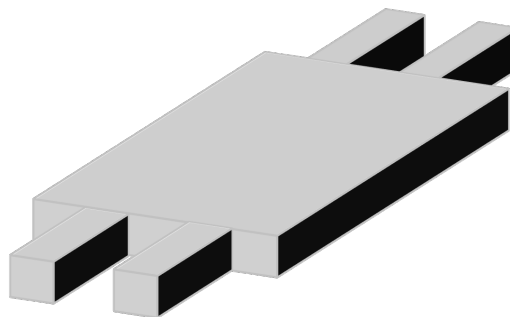


Figure 3.10: 2x2 splitter to be analysed.

As can be seen in the figure 3.10 this device will comprise of two inputs and two outputs. The design process for this MMI is as follows.

First, a width of 3.5 μm will be set for the splitter. This width value has been chosen to provide some margin in case it become necessary to introduce tapers to the MMI. Once the width value has been set, the length of the MMI to be simulated is calculated using the following expression.

$$L_{MMI_{2x2}} = \frac{3}{2} * L_{\pi} \quad (3.6)$$

Where $L_{MMI_{2 \times 2}}$ has the following expression:

$$L_{MMI_{2 \times 2}} = \frac{\lambda}{2|n_{eff0} - n_{eff1}|} \quad (3.7)$$

To determine the values of n_{eff0} and n_{eff1} , the silicon waveguide (Si) needs to be simulated for a width of $3.5 \mu m$, obtaining values of $n_{eff0} = 2.980$ and $n_{eff1} = 2.962$. Once these indices are calculated, the value of $L_{MMI_{2 \times 2}}$ can be determined with the expression 3.7 obtaining a value of $36.38 \mu m$, by using the expression 3.6 the required length for the MMI is $54.58 \mu m$.

After determining the required length for the MMI, it will be simulated as shown in the figure below:

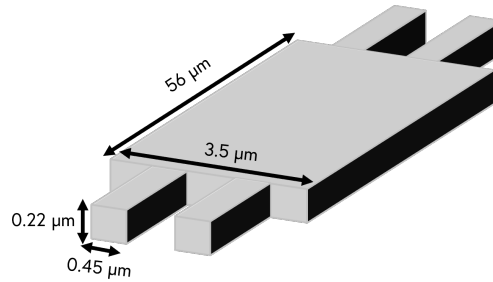


Figure 3.11: 2x2 splitter to be analysed with the fixed dimensions.

As observed in the above figure, a value of $56 \mu m$ has been chosen based on several iterations to optimize this parameter. Therefore, next a simulation with the parameters mentioned above will be carried out.

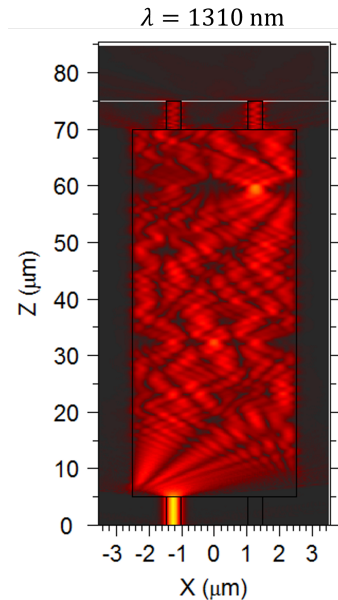


Figure 3.12: 2x2 splitter to be analysed with the fixed dimensions.

As can be seen in the previous image, the obtained results are not as desired, as the power dis-

tribution between the two output ports is not fifty-fifty divided. It is necessary that the power be divided 50/50 between the two output ports, so a taper will be inserted into the waveguide in order to achieve insertion and excess losses of approximately 3 dB. The waveguide has a width of $3.5\ \mu\text{m}$, a taper will be inserted with a width of $1\ \mu\text{m}$ and a length of $5\ \mu\text{m}$. This will result in a gap from the waveguide of $0.75\ \mu\text{m}$, next, an image of the structure to be simulated are shown.

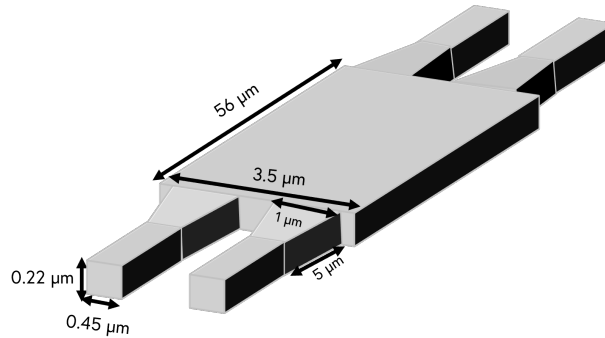


Figure 3.13: Final structure of the 2x2 splitter with taper.

This device has been simulated through RSoft, obtaining the following results.

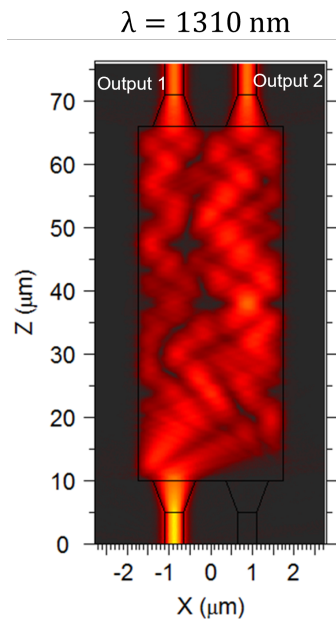


Figure 3.14: 2x2 splitter simulation result.

As can be seen in the figure above, using the structure of the 3.13 the result is an MMI where the power entering through port 1 is distributed equally between the two output ports, thus obtaining the desired functionality for the switch.

A summarised table of the parameter values to be used is shown below.

Length	Width	Taper length	Taper width end	Waveguide gap
56 μm	3.5 μm	5 μm	1 μm	0.75 μm

Table 3.1: Dimensions of the 2x2 splitter to be simulated.

Once the parameter values to be used have been determined, we will now analyse the insertion loss, excess loss, and imbalance for the frequency band O, which includes the frequency range of [1260-1360] nm.

Firstly, the insertion losses have been calculated using equation 3.3, obtaining the following graph:

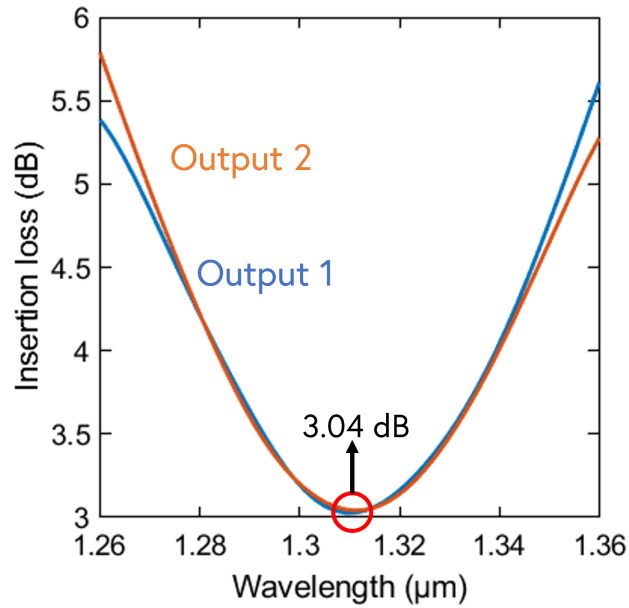


Figure 3.15: 2x2 splitter insertion losses.

As shown in figure 3.15 the insertion losses at the working wavelength (1310 nm) are close to 0 dB.

Secondly, the excess losses have been calculated using the following expression:

$$EL = |10\log_{10}\left(\frac{P_{out1} + P_{out2}}{P_{in}}\right)| \quad (3.8)$$

The graph is as follows:

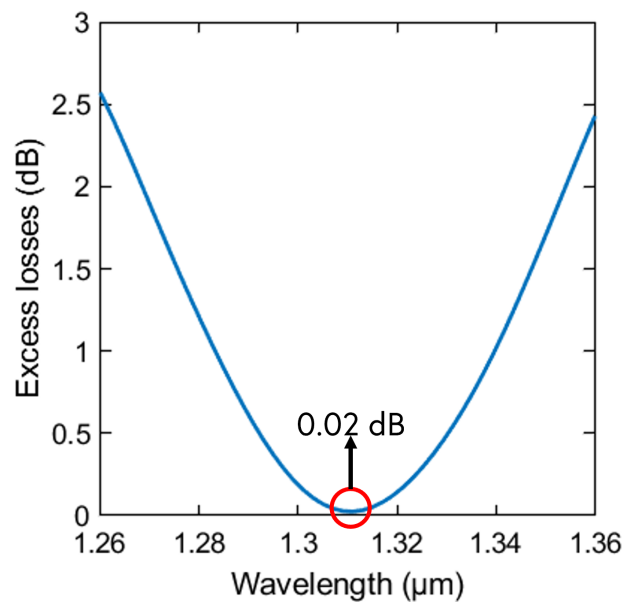


Figure 3.16: 2x2 splitter excess losses.

Looking at the graph above, it can be observed that the excess losses are practically 3 dB at 1310 nm.

Finally, the imbalance parameter will be analysed using the following expression.

$$PI = \left| 10 \log_{10} \left(\frac{P_{out1}}{P_{out2}} \right) \right| \quad (3.9)$$

The graph obtained is as follows:

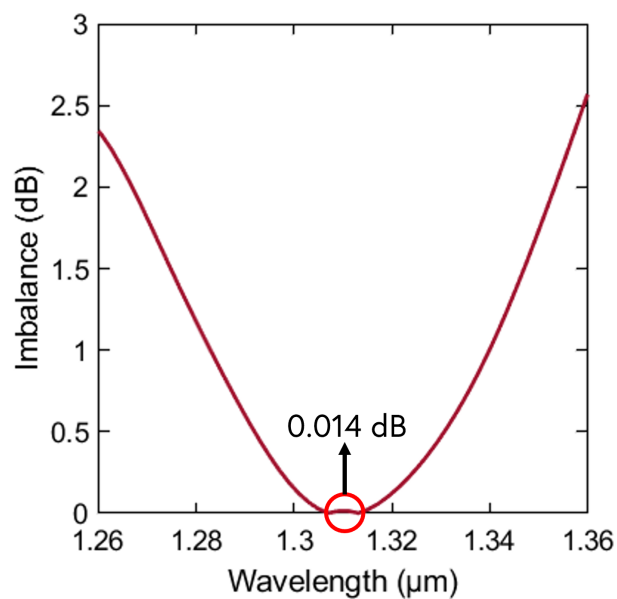


Figure 3.17: 2x2 splitter imbalance.

Similar to the other two parameters studied, the imbalance at 1310 nm obtained is negligible.

3.3 Design of grating couplers for fiber coupling

In this section, we will discuss the design process of the grating coupler that has been used to fabricate the switch described in previous sections.

An illustration of the design of the grating coupler is shown below.

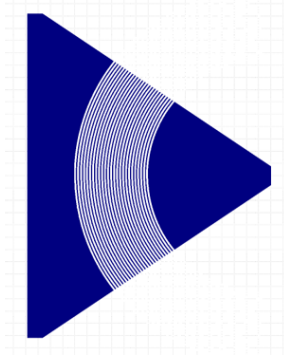


Figure 3.18: Schematic of the grating coupler.

Once the final appearance of the grating coupler has been shown, we will proceed to explain the design process that was followed. Understanding the main attributes that the grating's design require is crucial:

- TE polarization
- 1310 nm central wavelength
- 10° fiber angle

First of all, the effective index of the 220 nm slab needs to be calculated, which will be designated as n_{eff1} , the effective index of the shallow etched region with thickness of 70 nm will be denoted as n_{eff2} . The effective index of the grating can be calculated using the following expression:

$$n_{eff} = ff * n_{eff1} + (1 - ff) * n_{eff2} \quad (3.10)$$

The effective index for a 220 nm slab for a $\lambda = 1310$ nm is determined to be $n_{eff1} = 2.98$. Additionally, the effective index of the shallow etched region with thickness of 70 nm is $n_{eff2} = 2.68$. As an initial design, a fill factor is selected $ff = 50\%$. Using this fill factor, the weighted-average effective index of the grating, n_{eff} is 2.83.

After calculating the weighted-average effective index of the grating coupler, the next step is to determine the grating period, which can be calculated using the following expression:

$$\Lambda = \frac{\lambda}{n_{eff} - \sin(\theta_{air})} \quad (3.11)$$

With an incident angle of $\theta = 10^\circ$, the period of the grating can be calculated with the expression 3.11, the calculated grating period is approximately $\Lambda = 0.493 \mu m$.

Once the main grating parameters have been calculated, the next step is to optimise them.

First, the pitch value to be used in the design needs to be chosen.

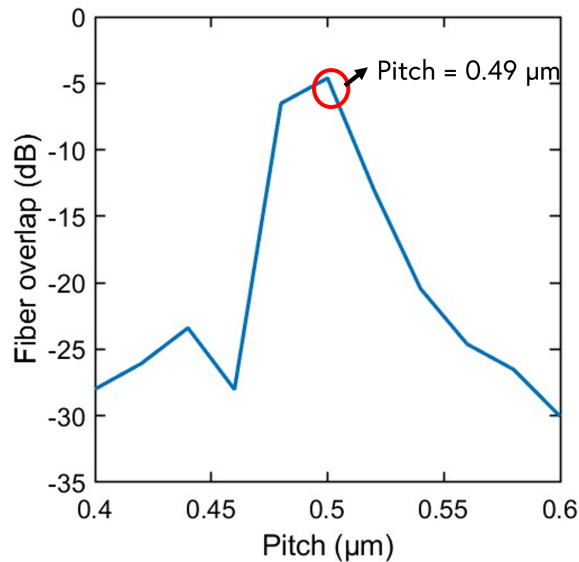


Figure 3.19: Pitch of the grating coupler.

Using RSoft's MOST tool, a sweep was performed by varying the pitch value from $0.4 \mu m$ to $0.6 \mu m$. As in figure 3.19, the lowest overlap value is obtained for a pitch of $0.49 \mu m$.

Once the pitch value has been set for $0.49 \mu m$, a sweep was performed to confirm if the value of the fill factor is still optimal for the design. The sweep was carried out for a range from 0 to 1, obtaining the following graph.

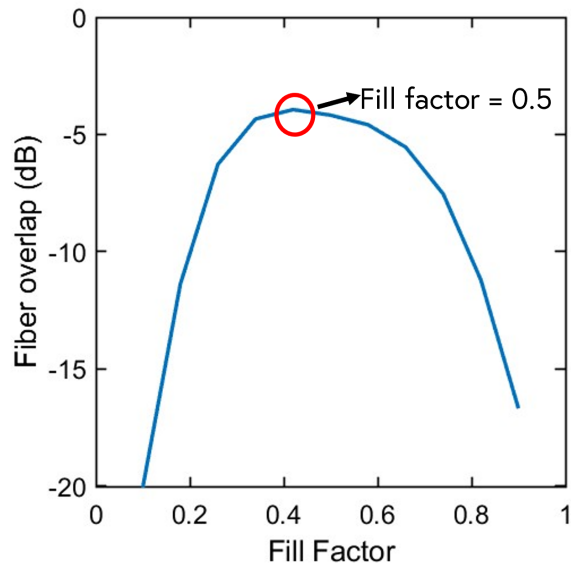


Figure 3.20: Fill factor of the grating coupler.

As can be seen in the graph above, it is confirmed that a fill factor of 50% remains optimal once the pitch variable is fixed.

Finally, the overlap obtained in the grating coupler was calculated for a $\lambda = 1310$ nm, as shown in the graph below.

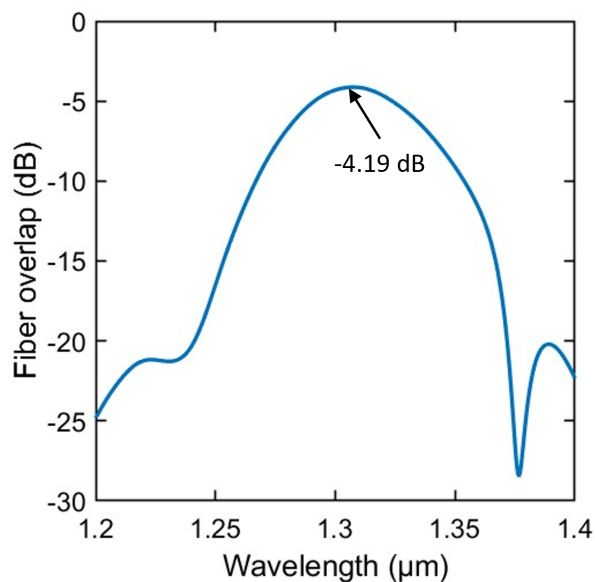


Figure 3.21: Overlap of the grating coupler.

In figure 3.21, the overlap obtained for the grating coupler is -4.19 dB at a wavelength of 1310 nm. Once the design process has been completed, a summary table of the parameters used in the design



of the grating.

Type	Pitch	Fill Factor	Etch-depth	Fiber angle
Focusing	490 nm	50%	70 nm	10°

3.4 Summary of final design

In conclusion, the aim of this chapter was to explain how the switch has been designed from the previously designed phase shifter. The several elements of the switch have been described. It was also possible to estimate the losses for the different state, which were estimated to be 0.07 dB for the bar state and 0.06 dB for the cross state. In addition, it was explained how the design process was carried out for the other elements that integrate the switch, such as: bend, MMI and grating coupler.

Based on the analysis and design processes presented, it has been determined that the optimum radius for the bend in the switch design is $5 \mu m$. Secondly, the design parameters for the MMI have been determined, with a length of $56 \mu m$ to achieving minimal losses. Finally, the grating coupler has been designed with an etch-depth of 70 nm, a fibre angle of 10° and a pitch of 490 nm to obtain coupling losses of -4.19 dB.

Chapter 4

Fabrication and experimental results

Next, in this chapter, we will explain the manufacturing process and the subsequently analysis of the results after measuring the sample.

The main characteristic of this manufacturing process is the use of Ma-N resist. The main objective of this chapter is to explain the electro beam lithography process using this type of resist.

For this purpose, a design at 1550 nm has been used. The first step to check if this type of resist is suitable for the designing devices at 1310 nm. We will then examine how the sample is distributed and the number of copies of the sample. It will explain which devices were used to measure the sample, and finally, it will examine at the results with MATLAB software.

4.1 Description of fabrication process

In this section, the manufacturing process is going to explain. The manufacturing technique used has been lithography, of the different types of lithography: electro beam lithography (EBL), Nanoimprint Lithography (NIL), Focused Ion Beam Lithography (FIB).

The technique used for the manufacture of this sample has been electro beam lithography (EBL). This technique uses a beam of highly fine electrons to create the patterns.

The difference between conventional lithography and EBL is that EBL uses high-energy electrons to perform the exposure and is capable of achieving high resolutions, i.e. on the nanometre scale; this advantage enables the manufacture of ultra-compact devices [11][12][13].

The process involved in electro beam lithography (EBL) consists of the following stages:

- **Sample preparation:** In this step you must choose the resist to be deposited on a silicon-on-insulator sample. The resist is deposited on 220 nm of silicon. This substrate is coated with a resist that is sensitive to electrons, and the resist used is called Ma-N2403. We used Ma-N2403 negative resist, which allows etching silicon with high resolution. One of the main advantages of this resist is the relatively low dose required for e-beam exposures reducing exposing times.
- **Entering the pattern:** The GDS file that has been designed is loaded into the system. As mentioned above, this file contains all the necessary information to control the beam during

the electron exposure.

- **Exposure:** The sample, which has been coated with resist in previous step, is carefully placed in the system. A beam with high-energy electrons is directed at the pattern introduced in previous steps.
- **Deposition and removal of the resist:** Once the exposure is done, the resist that has been exposed in the previous step must be removed. After the resist is removed, the pattern is deposited on the substrate using the material deposition process.

A summary image of this lithography process is presented below.

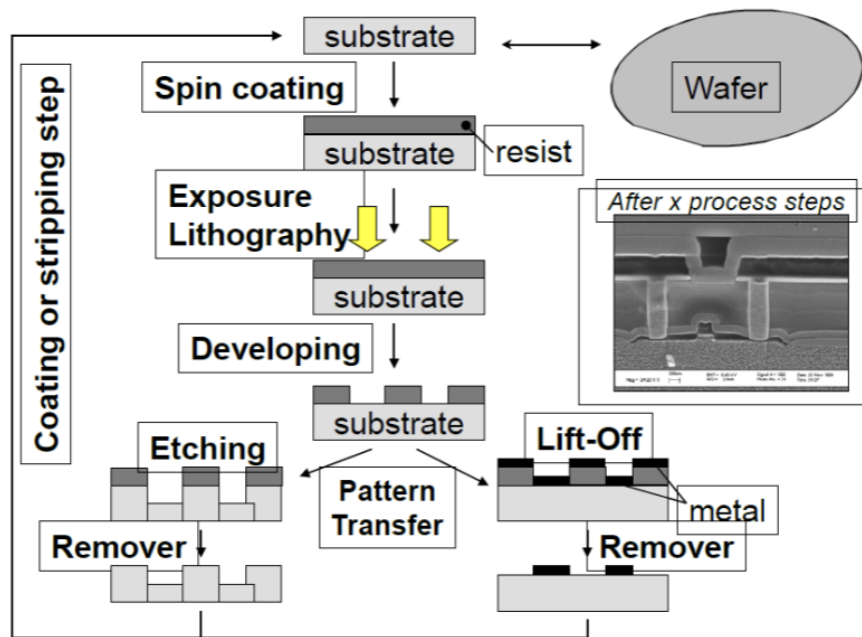


Figure 4.1: Schematic of electro beam lithography process [11].

4.2 Mask design of testing devices

The first step to carry out the study of the sample is the creation of the *Graphic Design System file*, GDS. This file provides the manufacturing team with information about the structures, shapes, dimensions of the desired layers, and the labels to be introduced in the sample to be manufactured. There are different programs that allow the creation of this GDS. In this work, we will use the program *KLayout*, which is a free program that allows the creation of GDS files. Next, we will show the GDS file that has been created and explain how the sample has been distributed in order to facilitate the analysis of the data.

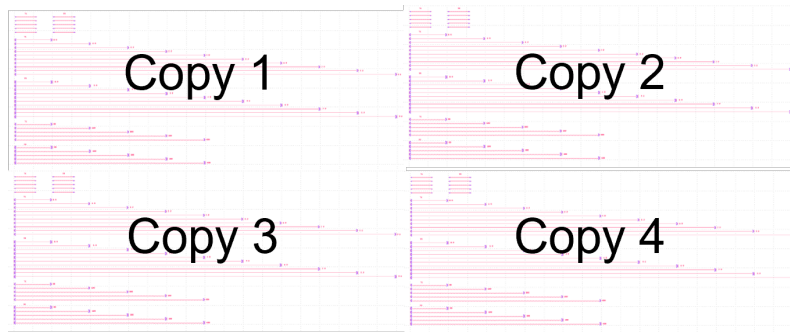


Figure 4.2: GDS structure of the sample to be tested.

As shown in figure 4.2, the sample contains four copies that will be analysed. The two upper copies will be referred to as Copy 1 and Copy 2, respectively, from left to right. On the other hand, the two lower copies will be named Copy 3 and Copy 4, also from left to right. The following section will explain in detail how are the copies distributed.

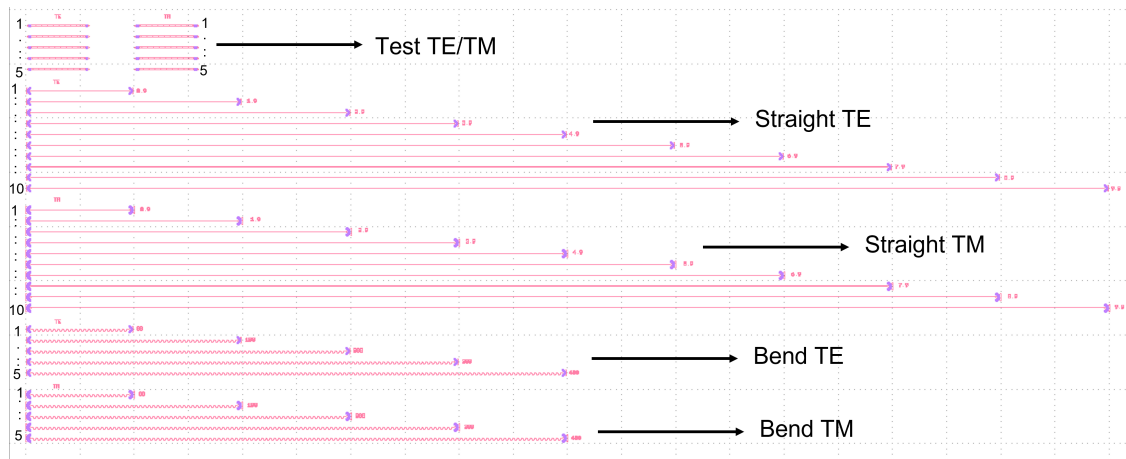


Figure 4.3: Detailed view of copy no. 1 of the sample to be analysed.

The layout is divided as follows, with replicas of each structure for TE and TM polarisation:

- **Test:** This structure is used to approximate the losses in the TE and TM polarization.
- **Straight:** This block is composed of linear gratings with a taper-to-taper distance of different lengths: 0.9, 1.9, 2.9, 3.9, 4.9, 5.9, 6.9, 7.9, 9.9. μm
- **Bend:** It is composed of grating connected by a curved waveguide with a different number of chained bends.

Once the GDS has been created and the sample has been manufactured, the next step is to select the set-up to be used for the characterisation of the sample.

4.3 Selection of experimental set-up

Next, we will explain the set-up used. The instruments used can be divided into two parts. Firstly, a microscope was used for the initial inspection of the sample. After a first inspection, the sample was transferred to the set-up.

The characterisation of the sample was measured with the following set-up.

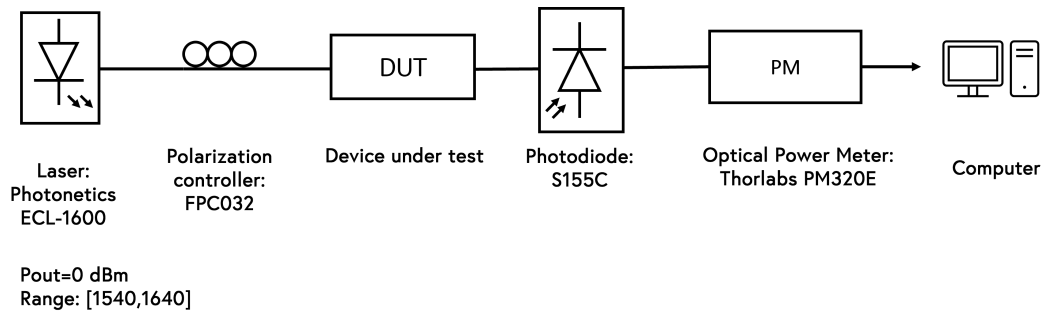


Figure 4.4: Setup for characterisation of the sample (Schematic).

As shown in figure 4.4 the first instrument used is the Photonetics ECL-1600 laser. This laser operates in the range of 1540 nm to 1640 nm, then the polarise is needed to control the TE and TM polarisation and achieve maximum power. Once the light has passed through the polarise the device under test is found. The measurements are performed using the Optical Power Meter (S155C and Thorlabs PM320E).

Everything described above is controlled by a LabView program developed by the NTC team. This software allows scanning from the range 1540 nm to 1640 nm, and the output power is measured in dBm units. All the data is compiled in a *.txt* file, which will be further processed using MATLAB software.

4.4 Experimental results

In the following section, we will present the experimental data obtained after the measurement process. These experimental data can be divided into two parts: inspection of the measurement and characterisation of the measurement with the set-up.

Firstly, the images collected by optical microscope will be presented.



Figure 4.5: Inspection through the microscope of the TE test structure of copy 1.

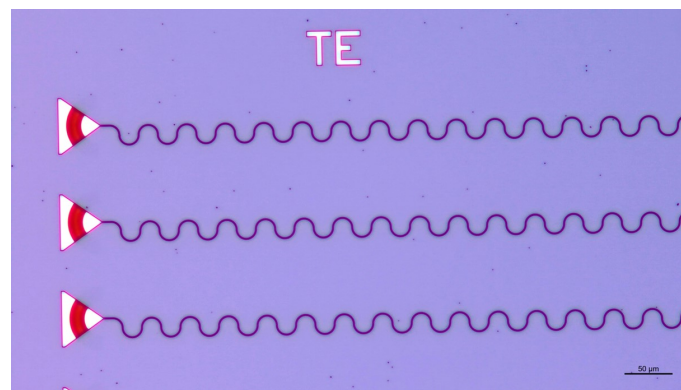


Figure 4.6: Inspection through the microscope of the TE bend structure of copy 1.

In the figure 4.5 it can be observed which is the appearance of the test structure for the TE polarization. On the other hand, in figure 4.6 the structure of the curved waveguides, as well as the straight waveguides, are formed with gratings at the beginning and end. In the following figure will be shown an image related to this.

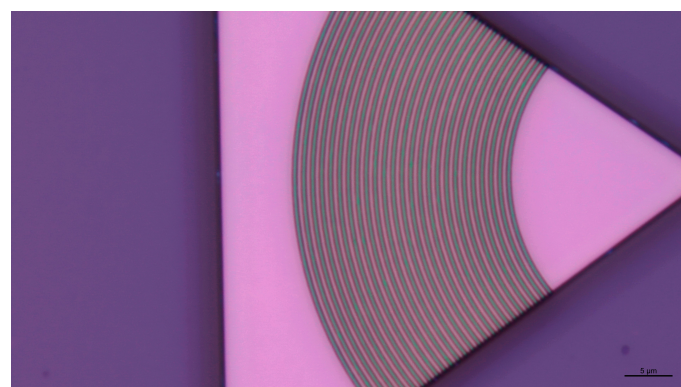


Figure 4.7: Inspection through the microscope of the grating structure of copy 1.

Once the initial inspection of the sample has been completed using the microscope, it is passed to

the set-up to the characterisation process. As mentioned before, the TE and TM test structures are employed to estimate the losses in each polarisation.

The next step involves characterising each structure of the sample.

We will focus on TE polarization, which is the chosen polarization for the designed Sb_2Se_3/Si switch. Therefore, we will first characterise the structure below.

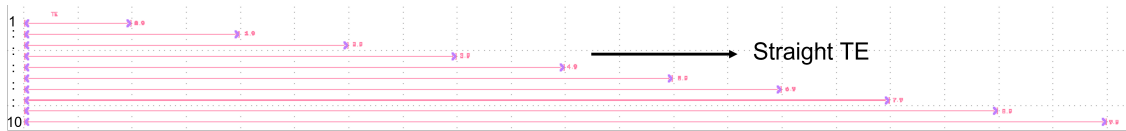


Figure 4.8: GDS image for the straight TE polarisation structure.

Each straight waveguide has been characterised for the different lengths shown in figure 4.8. The subsequent analysis of the characterised waveguide data yields the following results.

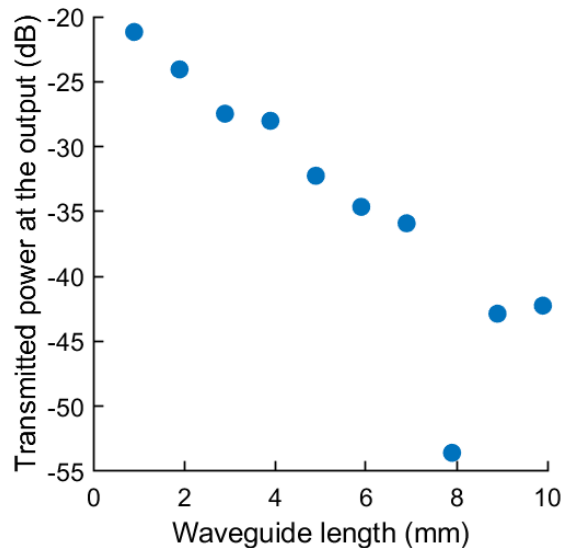


Figure 4.9: Analysis of propagation losses as a function of waveguide length for the straight structure in TE polarisation.

From the data obtained in figure 4.9, a linear regression will be performed to obtain the losses of the waveguide as well as the losses of the gratings.

The following linear regression expression will be used:

$$loss = a * l + b \quad (4.1)$$

Where $a \equiv$ propagation losses per unit length and $l \equiv$ length. Obtaining the following results:

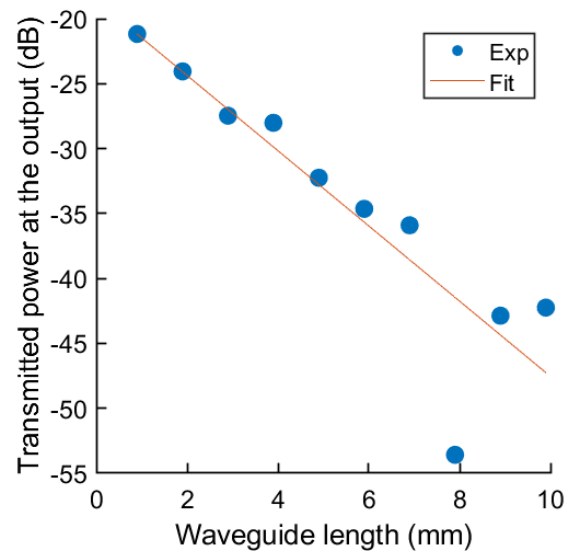


Figure 4.10: Linear fit of propagation losses of waveguide length for the straight structure in TE polarisation.

It should be considered that the measurement of the waveguide length 8 mm is not taken into account. This is because the measurement deviations observed in this particular case are attributed to causes other than propagation losses of the waveguide, such as cuts or defects in the coupling structure and would affect the final result of the linear regression.

Losses	Grating coupler losses
2.45 dB/mm	9.75 dB

Table 4.1: Results of straight waveguide losses and grating couplers for TE polarisation.

As shown in the table 4.1 grating coupler losses are relatively close to the simulated values (around 5-6 dB) while propagation losses should be improved.

In conclusion, this section has described the manufacturing process used to test the application of a new resist called Ma-N in lithography. Future steps would involve generating the corresponding GDS for the same building block at a $\lambda = 1310$ nm and to repeat and optimize the fabrication process.

Chapter 5

Conclusions and future work

5.1 Conclusions

This project aimed to develop a photonic switch using Sb_2Se_3 , a phase change material known for its significant index change between states and negligible imaginary part. The non-volatile nature makes it highly promising for integrated photonic devices.

First of all, a phase shifter was designed, which consisted of a silicon waveguide with dimensions of: $450\text{ nm} \times 220\text{ nm}$, and on top of it a layer of Sb_2Se_3 of thickness 40 nm was deposited. This device is intended to achieve a phase shift between its two states. Through several simulations, it was determined that a length of $6.6\ \mu\text{m}$ is required to obtain a phase shift of π between states. This phase transition between states would be carried out by a heater made of ITO material. Increasing the temperature of the heater, as mentioned in chapter one, enables the state changes. After determining the length of the phase shifter, the obtained losses were analysed and found to be 0.042 dB.

Following this, a description of the main objective of this work is provided, which was to realise a switch using the phase shifter mentioned above. To achieve this, it was necessary to design different basic building block such as bend, MMI and grating coupler. Once the design process of each of the elements that integrate the switch has been explained, the next step is to analyse the losses obtained in each state of the switch, which were found to be around 0.07 dB.

Finally, the manufacturing and measuring processes have been performed. In this manufacturing process, a special new feature was introduced, which is the use of a photo-resist called Ma-N. This resist has the main advantage of optimising the lithography process. Therefore, in this work, the characterisation of building blocks at 1550 nm has been carried out in order to assess the performance of the new resist in terms of optical losses.

To sum up, the new approach presented in this master's thesis for developing efficient communication systems has produce positive results. The design of the phase shifter and switch has performed well in the conducted test, surpassing the initial expectations. Therefore, it can be concluded that the main objective of this master's thesis has been successfully accomplished.



5.2 Future work

As future work, there are two main lines for further improvements. Firstly, the manufacturing and characterisation of the developed photonic device. This involve the creation of the corresponding GDS file for each of the blocks that have been explained in previous chapters, followed by their subsequent characterisation.

Secondly, the measurement process should be optimised by using the Ma-N resist for building blocks designed at 1310 nm. Further measurements should be conducted to refine the process and achieve optimal results.

References

- [1] S. Abdollahramezani, O. Hemmatyar, H. Taghinejad, *et al.*, *Nanophotonics*, vol. 9, no. 5, pp. 1189–1241, 2020. DOI: doi : 10 . 1515 / nanoph - 2020 - 0039. [Online]. Available: <https://doi.org/10.1515/nanoph-2020-0039>.
- [2] P. Sanchis Kilders, *Fundamentals of photonic integrated waveguides*. Universitat Politècnica de València, 2022, p. 45.
- [3] L. Chrostowski, *Silicon photonics design*. University Printing House, 2015, p. 439, ISBN: 978-1-107-08545-9. [Online]. Available: www.cambridge.org/chrostowski.
- [4] J. Hu, X. Sun, A. Agarwal, and L. C. Kimerling, “Design guidelines for optical resonator biochemical sensors,” *J. Opt. Soc. Am. B*, vol. 26, no. 5, pp. 1032–1041, May 2009. DOI: 10 . 1364 / JOSAB . 26 . 001032. [Online]. Available: <https://opg.optica.org/josab/abstract.cfm?URI=josab-26-5-1032>.
- [5] M. Iqbal, M. A. Gleeson, B. Spaugh, *et al.*, “Label-free biosensor arrays based on silicon ring resonators and high-speed optical scanning instrumentation,” *IEEE Journal of Selected Topics in Quantum Electronics*, vol. 16, no. 3, pp. 654–661, 2010. DOI: 10 . 1109 / JSTQE . 2009 . 2032510.
- [6] J. Parra, J. Hurtado, A. Griol, and P. Sanchis, “Ultra-low loss hybrid ito/si thermo-optic phase shifter with optimized power consumption,” *Opt. Express*, vol. 28, no. 7, pp. 9393–9404, Mar. 2020. DOI: 10 . 1364 / OE . 386959. [Online]. Available: <https://opg.optica.org/oe/abstract.cfm?URI=oe-28-7-9393>.
- [7] U. Nations, *17 sgds*, <https://sdgs.un.org/goals>, May 2015.
- [8] M. Delaney, I. Zeimpekis, D. Lawson, D. W. Hewak, and O. L. Muskens, “A new family of ultralow loss reversible phase-change materials for photonic integrated circuits: Sb₂S₃ and sb₂se₃,” *Advanced Functional Materials*, vol. 30, no. 36, p. 2 002 447, 2020. DOI: <https://doi.org/10.1002/adfm.202002447>.
- [9] D. Lawson, D. W. Hewak, O. L. Muskens, and I. Zeimpekis, “Time-resolved reversible optical switching of the ultralow-loss phase change material sb₂se₃,” vol. 24, no. 6, p. 064 013, May 2022. DOI: 10 . 1088 / 2040 - 8986 / ac5ece.
- [10] Y. Fei, Y. Xu, D. Huang, *et al.*, “On-chip reconfigurable and ultracompact silicon waveguide mode converters based on nonvolatile optical phase change materials,” *Nanomaterials*, vol. 12, no. 23, p. 4225, 2022.
- [11] U. D. Zeitner, M. Banasch, and M. Trost, “Potential of E-beam lithography for micro- and nano-optics fabrication on large areas,” *Journal of Micro/Nanopatterning, Materials, and Metrology*, vol. 22, no. 4, p. 041 405, 2023. DOI: 10 . 1117 / 1 . JMM . 22 . 4 . 041405.



- [12] U. D. Zeitner, M. Banasch, and M. Trost, *The potential of e-beam lithography for micro- and nano-optics on large areas*, J. A. Liddle and R. Ruiz, Eds. SPIE, 2023, vol. 12497, p. 1 249 703. DOI: 10.1117/12.2658440.
- [13] “Nanoimprint lithography for nanomanufacturing,” D. L. Andrews, R. H. Lipson, and T. Nann, Eds., pp. 357–386, 2019. DOI: <https://doi.org/10.1016/B978-0-12-803581-8.10508-9>.
- [14] *Photonic Solutions FemSIM FEM*. Synopsys, 2021, p. 114.
- [15] *Photonic Solutions FullWAVE FDTD*. Synopsys, 2021, p. 314.

Part II

Appendix

Appendix A

Simulation with FemSIM

FemSIM is a tool of RSoft, this tool provides the indices for 1D or 2D structures, for this a non-uniform hybrid mesh is used, in order to calculate these modes it is necessary to control different parameters such as: computational domain, grid sizes, boundary conditions, and other mesh properties. [14]

Firstly, to carry out the simulation of any structure, a simulation area must be defined, depending on the type of structure you have, a different coordinate must be set, in this work all simulations performed in FemSIM have been 2D structures so the Z position must be fixed and set up the simulation grid at the X and Y positions, as shown in the following figures.

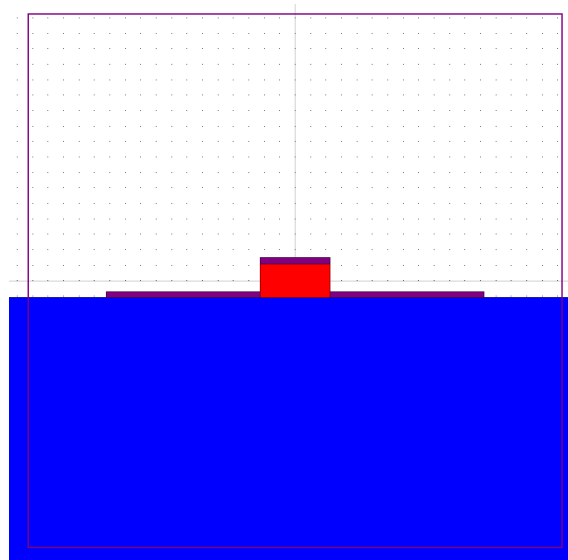


Figure A.1: Simulation area of the 2D structure simulated in FemSIM.

The figure A.1, it can be seen that after having set the limits in the X and Y positions, the simulation area will be the inside of the purple box.

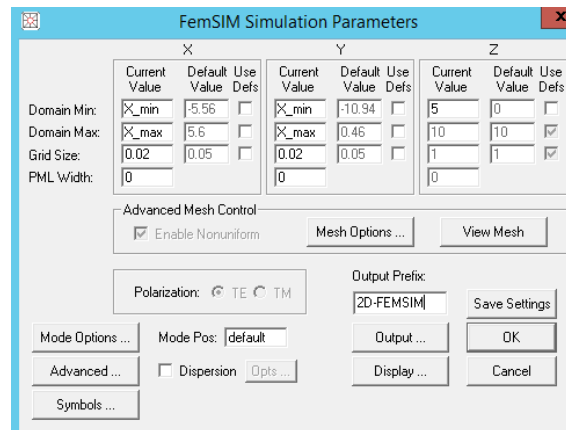


Figure A.2: Required parameters to configure in FemSIM.

In this figure A.2 it can be seen how the upper and lower limits of the positions to be varied have to be defined, for this reason any structure to be simulated must be within the parameters, on the other hand the parameter Grid Size this option sets the mesh size that will be generated in the simulation, it must be taken into account that FemSIM uses a non-uniform and irregular mesh, in this case a grid size of 20 nm has been used.

Another point to take into account is the mesh options section.

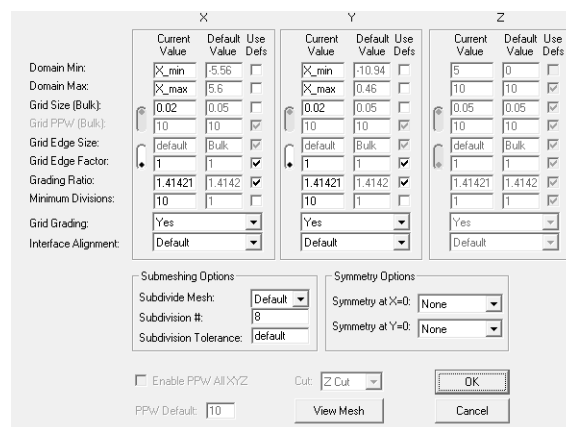


Figure A.3: Mesh options parameters to configure in FemSIM.

The most important parameter among the mesh options is the minimum number of divisions, this parameter indicates the minimum number of subdivisions that are desired in the mesh, in this work the minimum number of divisions that it is desired is 10 points.

Once all the important FemSIM parameters have been configured, the following mesh simulation is obtained.

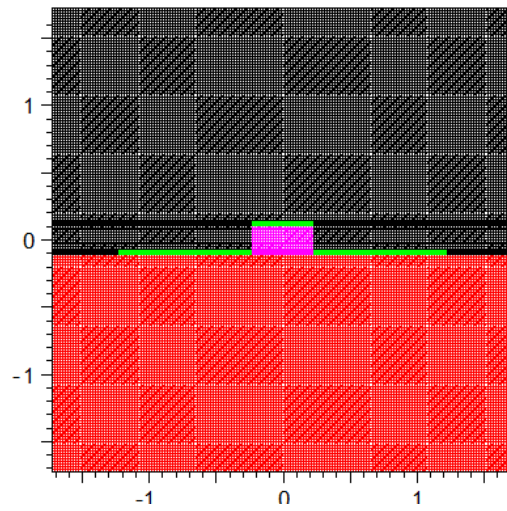


Figure A.4: Result of the mesh, after setting the necessary parameters.

In the figure A.4 the mesh is divided into different colours, in which each colour corresponds to a different material, in this way in violet there is silicon (Si) and in green the phase change material (Sb_2Se_3).

Appendix B

Simulations with FullWAVE

In the following, this appendix will explain the simulation procedure for FullWAVE. Like FemSIM, FullWAVE is an Rsoft tool that allows the electromagnetic calculation as a function of time and distance in response to the introduction of an electromagnetic excitation [15].

B.0.1 Spatial domain grid sizes

In contrast to FemSIM, which was a 2D structure, FullWAVE is a 3D structure, which means that the X, Y and Z positions are variable.

The simulation procedure is similar to the one explained in the previous appendix, except for some aspects. First of all, the simulation area of the structure must be defined, in this case it will be the one shown below:

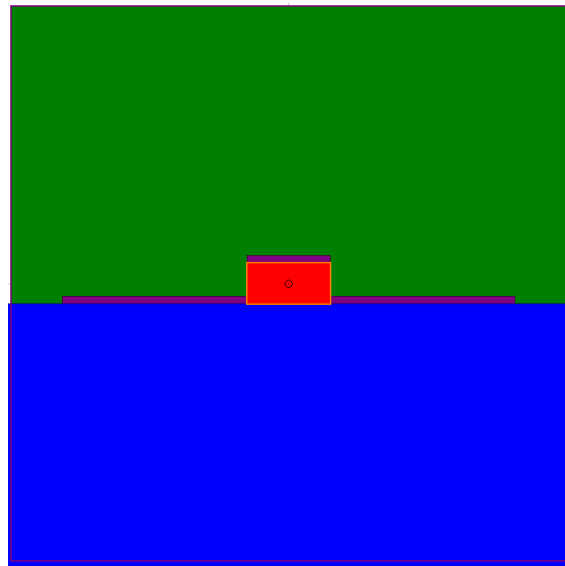
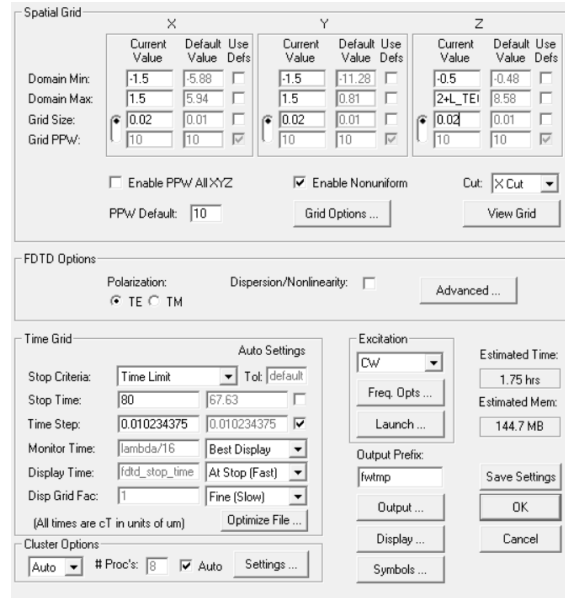


Figure B.1: Simulation area of the designed structure.



Spatial Grid

	X			Y			Z		
	Current Value	Default Value	Use Defs	Current Value	Default Value	Use Defs	Current Value	Default Value	Use Defs
Domain Min:	-1.5	-5.98	<input type="checkbox"/>	-1.5	-11.28	<input type="checkbox"/>	-0.5	-0.48	<input type="checkbox"/>
Domain Max:	1.5	5.94	<input type="checkbox"/>	1.5	0.81	<input type="checkbox"/>	2+L_TET	0.58	<input type="checkbox"/>
Grid Size:	0.02	0.01	<input type="checkbox"/>	0.02	0.01	<input type="checkbox"/>	0.02	0.01	<input type="checkbox"/>
Grid PPW:	10	10	<input checked="" type="checkbox"/>	10	10	<input checked="" type="checkbox"/>	10	10	<input checked="" type="checkbox"/>

Enable PPW All XYZ Enable Nonuniform Cut: X Cut
 PPW Default: 10 Grid Options ... View Grid

FDTD Options

Polarization: TE TM Dispersion/Nonlinearity: Advanced ...

Time Grid

Stop Criteria: Time Limit Tot: default
 Stop Time: 80 67.63
 Time Step: 0.010234375 0.010234375
 Monitor Time: lambda/16 Best Display
 Display Time: fidd_stop_time At Stop (Fast)
 Disp Grid Fac: 1 Fine (Slow)
 (All times are cT in units of um) Optimize File ...

Excitation

Excitation: CW
 Freq. Opts ...
 Launch ...
 Output Prefix: fwtmp
 Output ...
 Display ...
 Symbols ...

Estimated Time: 1.75 hrs
 Estimated Mem: 144.7 MB
 Save Settings OK Cancel

Cluster Options

Auto # Proc's: 8 Auto Settings ...

Figure B.2: Configuration of spatial domain and grid size parameters.

As in the previous appendix, the minimum and maximum limits of the X, Y and Z positions must be established, as well as the Grid size to be used, in this case, as can be seen in the following figure, it will be 20 nm, this parameter has been chosen depending on the materials used, the working wavelength, the expression used to find the grid size value is as follows.

$$x = \frac{\lambda}{n_{eff}} \quad \text{---} > \text{Points} = \frac{x}{15} \quad (\text{B.1})$$

After setting all the parameters discussed above, it is possible to get the index profile, which provides us with a CountourMap of the XY, XZ and YZ sections, which will help us to check that the refractive index is correct for each designed segment, an example of which can be seen below.

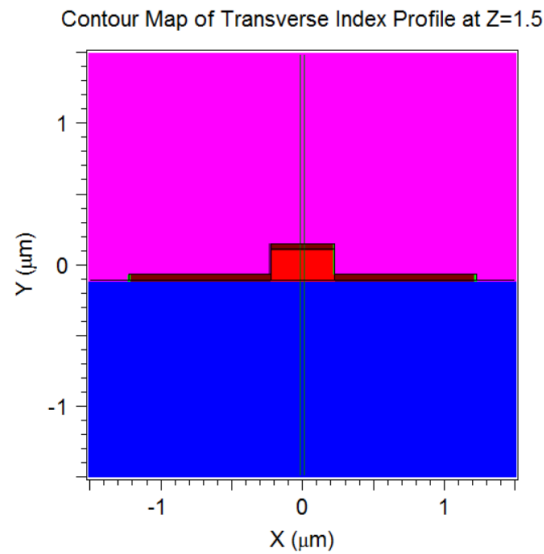


Figure B.3: A sample non-uniform of the waveguide. A fine grid size of 20 nm is used.

B.0.2 Time domain, time step and excitation

As mentioned at the beginning of the appendix, the main feature of FullWAVE is that it is able to resolve electromagnetic fields as a function of time [15], for this reason setting these parameters properly on the simulator is essential in order to obtain correct results.

The parameters to be configured can be seen below.

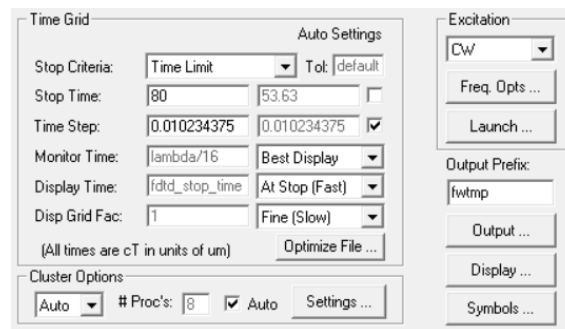


Figure B.4: Parameters to be configured time domain, time step and excitation.

The most important parameter is the stopping criteria, for this work we have used the criterion of *Time limit*, this criteria shall stop the simulation when it has reached the *Stop time* and disables auto-convergence automatically.

Another parameter to configure is the choice of excitation, there are two options, pulsed or continuous wave (CW), in this case a continuous wave will be used, the excitation needs a launch field, in this case the excitation for the simulation will be a straight silicon only waveguide at 1310 nm.

$$n_{\text{eff}} = 2.645$$

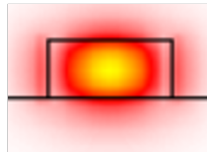


Figure B.5: Index of the guide used as a launch in the simulation.

Lastly, the configuration of the monitors is crucial for a good analysis of the data. There are different types of monitors, in the design have been introduced six monitors distributed as follows:

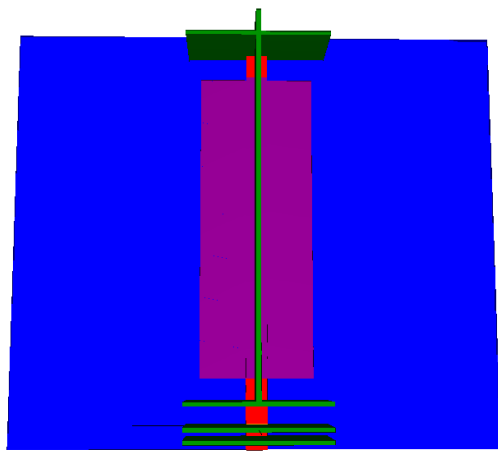


Figure B.6: Distribution of the monitors used in the structure.

There are different types of monitors within FullWAVE, in this design the following have been used. Firstly, at the beginning of the silicon waveguide, two monitors have been introduced with a separation between them of $0.5 \mu m$, the functionality of these two monitors is: the first one is an Overlap Power type, this monitor will indicate the possible reflections that may have been produced once the launch has been launched, the second monitor is of type *Spatial* has the characteristic that it is recorded at specific time intervals determined by the Spatial Output Time parameter specified [15], this monitor has been configured to measure the field in the X-coordinate, that is the field E_x , near the beginning of the hybrid guide has been introduced that measures the overlap of the introduced launch, transversal to the hybrid waveguide there is a monitor that will allow us to know the field. E_x and finally, a monitor has been introduced once the hybrid waveguide has passed, which will indicate the behaviour of the field once the hybrid waveguide has finished.